

For sky-facing passive radiative cooling, are wavelength-selective emitters the best choice?

Yeonghoon Jin¹ and Mikhail Kats^{1,2}*

¹Department of Electrical and Computer Engineering, University of Wisconsin-Madison, Madison, WI, USA

²Department of Material Science and Engineering, University of Wisconsin-Madison, Madison, WI, USA

E-mail: mkats@wisc.edu

Abstract

For passive cooling via thermal radiation toward the sky, it is known that an ideal selective emitter (SE) with high emissivity only in the 8–13 μm atmospheric transparency window can reach a lower equilibrium temperature than an ideal broadband emitter (BE) across the mid infrared. Here, we evaluate whether this principle should guide the development of practical passive radiative cooling technologies. We model and compare the cooling performance of sky-facing SEs and BEs at various locations on Earth, accounting for the distributions of atmospheric temperature and gas composition at specific dates and times. We find that for emitter temperatures at or higher than the ambient temperature, an ideal broadband emitter always provides higher net cooling power, while for sub-ambient cooling, an ideal selective emitter is usually slightly better, but the difference in cooling power is small, at most 1-2% of the incident solar power during daytime. Our conclusion is that large-scale deployment of passive radiative cooling technologies should focus on design and manufacturing of scalable low-cost surfaces with the lowest possible solar absorption without worrying too much whether the emitter is broadband or selective.

Passive radiative cooling with engineered surfaces can enable cooling power of up to 100~150 W/m² without external energy input, and is being considered as a component of a strategy of sustainability (1, 2). This technology is being explored in the context of paint (3-5), cooling of water and other working fluids (6, 7), textiles (8, 9), and solar-cell cooling (10-12). One major area of recent research has been ‘daytime radiative cooling’, where a thermal emitter radiates in the mid-infrared (IR) range but reflects most sunlight, such that significant cooling power and an equilibrium temperature below the ambient temperature can be achieved even under solar illumination (1). While it is evident that a passive-cooling thermal emitter should reflect the entire solar spectrum range (mainly 0.3–2.5 μm) as much as possible, the optimum thermal emissivity spectrum in the mid-IR range depends on the environment (2) and on the particular application.

The basic mechanism underlying most applications of radiative cooling is that an emitter radiates mid-IR photons to the sky, usually in the 3–25 μm wavelength range (**Figure 1a**, and also see **Figure S3**). A significant fraction of the photons emitted at wavelengths where atmospheric gases absorb weakly will be transmitted to cold outer space (which has a background temperature of ~3 K), generally through the atmospheric transparency window of 8–13 μm. In contrast, the vast majority of the photons emitted in the 5–8 and 13–25 μm ranges will be absorbed by atmospheric gases (mainly H₂O and CO₂), and these same gases also radiate thermal energy in all directions, including back toward the emitter, with intensity and spectrum given by the temperature of the gases and their infrared absorption spectra. It is evident that the 8–13 μm atmospheric window is the main cooling channel, but thermal emission at other wavelengths can also meaningfully contribute to cooling (4, 13), depending on the operating temperature of the emitter and other factors. Nevertheless, even recently, many papers—including some from our group—show and/or focus on the emissivity only in the atmospheric window (14-20) instead of the full mid-IR range of 3–25 μm.

It has been understood that a narrow-band selective emitter (SE) that shows high emissivity only at 8–13 μm (**Figure 1a**, black dashed line) can reach a lower equilibrium temperature when facing a clear sky, while a broadband emitter (BE) that shows high emissivity over the full 3–25 μm range (**Figure 1a**, red solid line) can reach a higher overall cooling power (2, 13). This is because wavelengths outside the atmospheric window (8–13 μm) primarily serve as heating channels when the temperature of an emitter is below the ambient temperature, whereas they primarily serve as cooling channels when the emitter temperature is higher than the ambient

temperature, with the cross-over temperature being slightly below the ambient temperature (**Supplementary Note 1**). However, the cooling performance of an emitter is significantly affected by various factors such as the temperature and gas composition of the atmosphere, solar absorption, and conduction and convection, and thus the cooling performance of the ideal emitters should vary substantially with location and time. In particular, the atmospheric temperature and gas composition, which vary with altitude as well as location and time, considerably affect the cooling performance. However, to our knowledge, these considerations have not been fully accounted for in the literature.

The community of researchers working on radiative cooling sometimes refer to general region types that have different atmospheric transparency, such as “tropical” and “mid-latitude summer” (14, 15, 18, 21, 22); however, the definitions of these regions are not so precise. In addition, a number of papers perform calculations assuming atmospheric transmittance (τ_{atm}) from the Gemini Observatory (23) located either at Mauna Kea in Hawaii (altitude of 4.2 km) or Cerro Pachon in Chile (altitude of 2.7 km) (22, 24-29). However, the Mauna Kea and Cerro Pachon τ_{atm} spectra are not suitable for accurately modeling passive radiative-cooling performance for most practical applications because atmospheric gases are much denser within a few kilometers of the Earth’s surface compared to the rest of the atmosphere, and therefore this low-altitude region should not be neglected. This is why τ_{atm} spectra obtained from the Gemini Observatory (23) are usually higher than those from other regions (compare **Figure S2** in **Supplementary Note 2** to **Figure 1b**). In addition, the ambient temperature (T_{amb}) measured near the ground has been generally used as the atmospheric temperature (27-30). However, the atmospheric temperature is generally lower than T_{amb} and decreases as the altitude increases within the troposphere (31). Fortunately, it is possible to account for all of these variables by using the NASA Planetary Spectrum Generator (PSG) (32), which provides planetary spectra by combining several radiative-transfer models with spectroscopic and planetary databases. In this paper, we rigorously estimate the cooling performance of ideal and realistic sky-facing emitters, both broadband emitters (BEs) and selective emitters (SEs), and systematically compare which emitter would be better in various locations on Earth.

Figure 1b shows the atmospheric transmittance (τ_{atm}) for five different regions where large-scale deployment of radiative cooling technologies may be desired. We used the NASA PSG to obtain τ_{atm} spectra in the Atacama Desert (69.13°W/23.86°S on Dec 1st, 2023, at 12 pm), Cairo

(31.24°E/30.04°N on Aug 1st, 2023, at 12 pm), Phoenix (247.93°E/33.45°N on Aug 1st, 2023, at 12 pm), Houston (264.63°E/29.76°N on Aug 1st, 2023, at 12 pm), and Singapore (103.82°E/1.35°N on May 1st, 2023, at 12 pm). The spectra we generated using the NASA PSG assume clear skies (*i.e.*, no clouds), which is a good assumption at those particular dates and times. See **Supplementary Note 2** for detailed instructions about how to use the PSG. The τ_{atm} spectra vary significantly by location: the humid tropical region, Singapore, exhibits the lowest τ_{atm} , while the arid area, the Atacama Desert, shows the highest τ_{atm} because of low humidity.

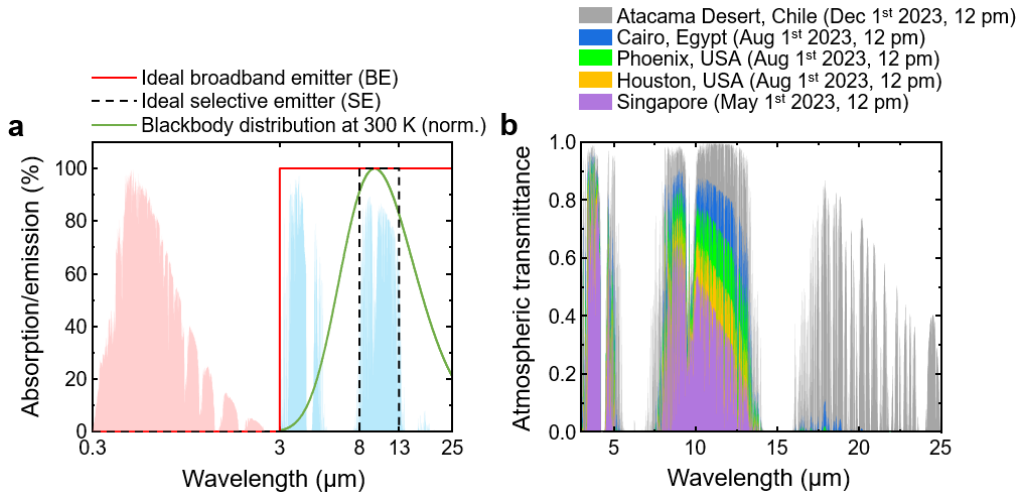


Figure 1. (a) Emissivity spectra of the ideal broadband emitter (BE) (red solid line) and the ideal selective emitter (SE) (black dashed line). The normalized blackbody distribution $B_{\lambda}(\lambda, T)$ at a temperature T of 300 K (green line). Normalized solar spectrum (pink shaded region) and atmospheric transmittance (light-blue shaded region) in Cairo (Aug 1, 2023, at noon). **(b)** Atmospheric transmittance (τ_{atm}) spectra of five selected regions on different dates (always at noon), which were obtained through the NASA PSG(32) (see **Supplementary Note 2** for detailed description).

Figure 2a shows the altitude-dependent temperature profile (where total atmospheric pressure is a proxy for altitude) and **Figure 2b** shows the atmospheric gas abundance (ratio with respect to the total pressure at a specific altitude) profiles, above Singapore on May 1st, 2023 at 12 pm, which were extracted from the Modern-Era Retrospective Analysis for Research and Applications, version 2, (MERRA-2) database (33) and accessed through the PSG (see **Supplementary Note 2**) (32). As shown in **Figure 2a**, the atmospheric temperature significantly varies with altitude, in particular decreasing with increasing altitude in the troposphere (from sea level to an altitude of ~15 km). This means the actual atmospheric temperature is colder than T_{amb} on the ground, so the potential cooling power is higher than if the atmospheric temperature is assumed to be equal to the ground temperature. The reduction of temperature at high altitudes has previously been pointed

out in the context of the temperature of the ozone layer (34). As the altitude increases, the atmospheric pressure also decreases and thus the density of atmospheric gases decreases. There are two main gases that strongly affect radiative cooling because of strong absorption in the mid-IR range: H₂O and CO₂. As shown in **Figure 2b**, H₂O vapor is concentrated within a few kilometers from the ground. The density of CO₂ also decreases with increasing altitude because the total pressure decreases, although the abundance (ratio with respect to the total pressure) of the CO₂ gas is almost constant with altitude.

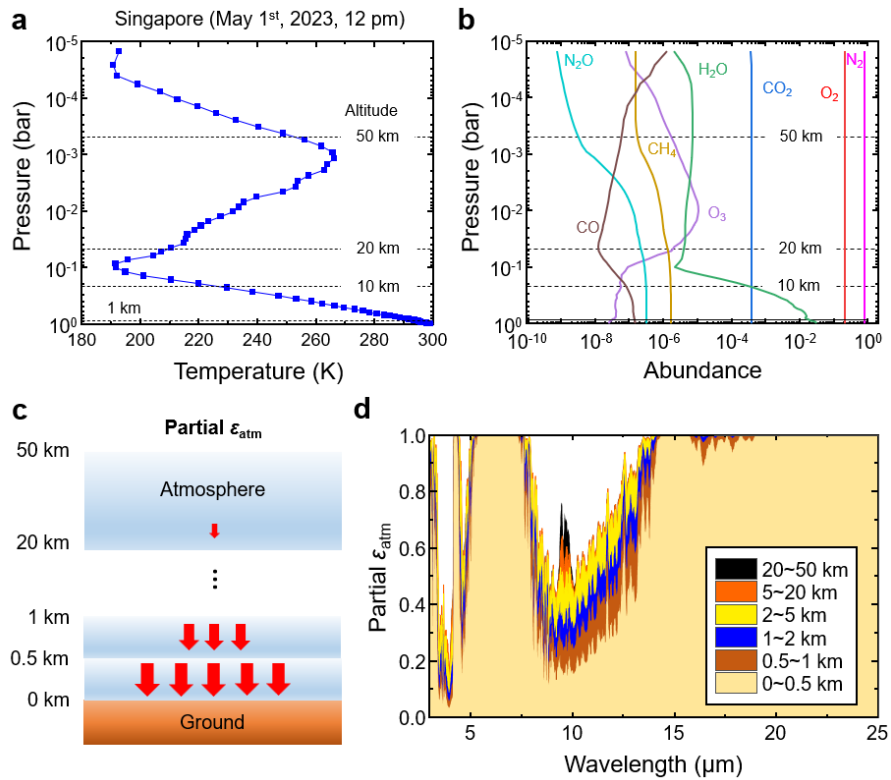


Figure 2. Atmospheric profiles as a function of altitude above Singapore (May 1st, 2023, noon). **(a)** Atmospheric temperature and **(b)** gas abundance (ratio with respect to the total pressure) profiles with respect to altitude, quantified by total pressure. **(c)** Schematic defining the partial atmospheric emissivity (ϵ_{atm}) from a specific atmospheric layer (e.g., ϵ_{atm} from 0~0.5 km above the ground). **(d)** The partial ϵ_{atm} from six atmospheric layers. Even at the bottom atmospheric layer (0~0.5 km from the ground), the ϵ_{atm} values at wavelengths of 5–8 and 14–25 μ m are close to unity, because atmospheric gases (H₂O and CO₂) are highly concentrated within a few kilometers from the ground. These data were obtained through the NASA PSG(32); see **Supplementary Note 2** for detailed explanation.

Based on the profiles in **Figures 2a** and **2b**, the partial atmospheric emissivity (ϵ_{atm}), which is defined by thermal emission that is radiated by a specific atmospheric layer (e.g., ϵ_{atm} from 0 to 0.5 km above the ground) and reaches the ground, as shown in **Figure 2c**, can be obtained. **Figure**

2d shows the partial ε_{atm} 0~0.5 km above the ground, 0.5~1 km, 1~2 km, 2~5 km, 5~20 km, and 20~50 km (more details in **Supplementary Note 2**). Because the total atmospheric pressure is very low at altitudes above 50 km (**Figures 2a** and **2b**), we can ignore any contribution to radiative heat transfer from the atmosphere above this point. Interestingly, the ε_{atm} spectrum even from the bottom-most atmospheric layer (0~0.5 km above the ground) is already ~ 1 at wavelengths of 5–8 and 14–25 μm , and the spectrum for the full mid-IR range is almost saturated at 5 km from the ground. This is because H_2O and CO_2 are concentrated within a few kilometers from the ground (**Figure 2b**). Accordingly, we can say that thermal emission from atmospheric gases mostly occurs within a few kilometers from the ground, and the atmospheric temperature higher than tens of kilometers from the ground is not important. In our calculations for this paper, we divided the atmosphere into 14 layers from 0~50 km from the ground; see **Supplementary Note 2** for detailed information.

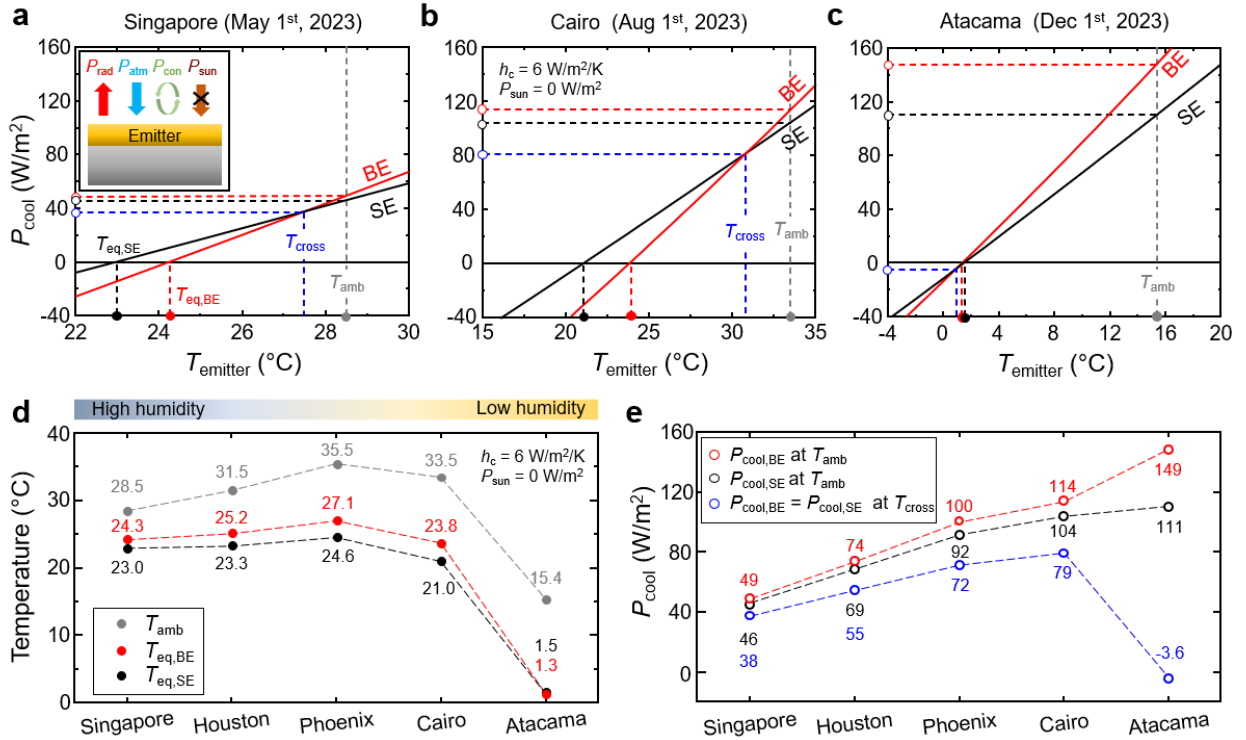


Figure 3. Evaluation of cooling performance of the ideal BE and SE in five selected regions, assuming no solar absorption by the emitter ($P_{\text{sun}} = 0 \text{ W/m}^2$). **(a-c)** The net cooling power (P_{cool}) of the ideal BE (red) and SE (black line) as a function of the emitter temperature (T_{emitter}) in **(a)** Singapore (May 1st, 2023), **(b)** Cairo (Aug 1st, 2023), and **(c)** the Atacama Desert (Dec 1st, 2023), all at noon. Summarized **(d)** temperature and **(e)** P_{cool} values in the five regions with varying humidity. T_{amb} is the ambient temperature on the ground; $T_{\text{eq,BE}}$ and $T_{\text{eq,SE}}$ are the equilibrium temperatures that the BE or SE reach assuming no thermal load (*i.e.*,

cooling only the emitter itself). T_{cross} is the temperature of the emitter at which the BE and SE have the same cooling power. The non-radiative heat transfer coefficient (h_c) was set to 6 W/m²/K.

By considering the above-mentioned atmospheric temperature and gas abundance profiles, we calculate the net cooling power (P_{cool}) of an emitter to evaluate the cooling performance. The net cooling power (P_{cool}) is defined by $P_{\text{cool}} = P_{\text{rad}} - P_{\text{atm}} - P_{\text{sun}} - P_{\text{con}}$, as depicted in the inset of **Figure 3a**: P_{rad} is the power radiated by the emitter, P_{atm} is the power emitted by atmospheric gases (from 14 atmospheric layers with different temperature of each layer) and then absorbed by the emitter, P_{sun} is the absorbed solar power, and P_{con} is the heat exchange through conduction and convection with the surrounding environment. $P_{\text{sun}} = 0$ in this case because an ideal radiative-cooling emitter should perfectly reflect the solar spectrum, as shown in **Figure 1a**. See **Supplementary Note 3** for detailed calculations of the overall power factors. We used a non-radiative heat transfer coefficient (h_c) of 6 W/m²/K, which quantifies the heat exchange via conduction and convection (P_{con}), because h_c in practical scenarios may be 6–11 W/m²/K (35), and we chose a conservative value.

Figures 3a-c show the net cooling power (P_{cool}) of the ideal BE (red line) and SE (black line) as a function of the emitter temperature (T_{emitter}) for an emitter facing the sky in Singapore (May 1st, 2023, at noon), Cairo (Aug 1st, 2023, at noon), and the Atacama Desert (Dec 1st, 2023, at noon), assuming no solar absorption by the emitters ($P_{\text{sun}} = 0$ W/m²). We first consider the case of the highest humidity and therefore lowest τ_{atm} : Singapore (**Figure 3a**). At noon on this day, the ambient temperature (T_{amb}) near the ground was 28.5 °C. The equilibrium temperature of the ideal BE ($T_{\text{eq, BE}} = 24.3$ °C), which is the temperature where P_{cool} becomes 0, is indicated by the red circle, and that of the ideal SE ($T_{\text{eq, SE}} = 23.0$ °C) is indicated by the black circle. Here, we would like to emphasize that the emitters are assumed to be placed on a thermal insulator, and they are cooling nothing beside themselves at the equilibrium temperatures; these T_{eq} values are the minimum achievable temperature, and would increase if the emitter was connected to a thermal load and was therefore providing a cooling benefit. The equilibrium temperature for both ideal emitters in Singapore is somewhat lower than the ambient temperature ($T_{\text{eq, BE}} = 24.3$ °C and $T_{\text{eq, SE}} = 23.0$ °C, given an ambient temperature $T_{\text{amb}} = 28.5$ °C). Notably, the difference between $T_{\text{eq, SE}}$ and $T_{\text{eq, BE}}$, $\Delta T_{\text{eq}} = T_{\text{eq, BE}} - T_{\text{eq, SE}}$, is only 1.3 °C.

The maximum net cooling power in the sub-ambient range (P_{cool} at T_{amb}) of the ideal BE ($P_{\text{cool, BE}}$) is 49 W/m², and that of the ideal SE ($P_{\text{cool, SE}}$) is 46 W/m² (**Figure 3a**). These values are

significantly lower than a potential cooling power of 100~150 W/m², because of the high humidity and the low atmospheric transmittance (τ_{atm}) in Singapore (**Figure 1b**). To compare the net cooling power (P_{cool}) between both emitters, it is useful to calculate P_{cool} at the crossing temperature ($T_{\text{cross}} = 27.5$ °C), where both emitters have the same P_{cool} , because this is the maximum cooling power at which the ideal SE can outperform the ideal BE. At this time in Singapore, P_{cross} is only 38 W/m², which means that the ideal SE is better than the ideal BE only if the achievable cooling power P_{cool} is lower than 38 W/m². Moreover, the difference in P_{cool} between the ideal emitters in the sub-ambient range is below 11 W/m². Given the small difference in cooling power and achievable temperature between the ideal BE and SE, we believe that the cheaper- and easier-to-fabricate emitter would usually be the better option for sub-ambient cooling.

Figure 3b shows the cooling performance of both ideal emitters in Cairo. The cooling performance in this location should be better than that in Singapore because the atmospheric transmittance (τ_{atm}) in Cairo is higher than that in Singapore: the equilibrium temperature of the ideal emitters ($T_{\text{eq,BE}} = 23.8$ °C and $T_{\text{eq,SE}} = 21.0$ °C) is 10~12 °C lower than the ambient temperature T_{amb} of 33.5 °C, and the net cooling power at T_{amb} of the ideal BE ($P_{\text{cool,BE}}$) is 114 W/m² and that of the ideal SE ($P_{\text{cool,SE}}$) is 104 W/m². Indeed, this location should be the most-suitable for the ideal SE compared to the ideal BE because of the high τ_{atm} at 8–13 μm and low τ_{atm} at 13–25 μm (**Figure 1b**).

Figure 3d shows the ambient and equilibrium temperatures (T_{amb} , $T_{\text{eq,BE}}$, and $T_{\text{eq,SE}}$) in the five selected locations and **Figure 3e** shows P_{cool} values in those locations. The difference in the equilibrium temperature between the ideal BE and SE, $\Delta T_{\text{eq}} = T_{\text{eq,BE}} - T_{\text{eq,SE}}$, is highest in Cairo, with $\Delta T_{\text{eq}} = 2.8$ °C (**Figure 3d**). Similarly, the highest power at which the ideal SE can outperform the ideal BE is also in Cairo: P_{cool} at T_{cross} is 79 W/m² (blue circles in **Figure 3e**). However, even in Cairo, ΔT_{eq} is lower than 3 °C, and the maximum difference in P_{cool} between the two emitters in the sub-ambient range is limited to 22 W/m², which corresponds to ~2% of solar absorption. Indeed, a practical operating temperature range of an emitter in most real-world applications is usually within a few degrees of T_{amb} (6, 7), and the difference in P_{cool} between the two emitters in this temperature range is small (**Figure 3b**).

Unlike in other four regions that we considered, in the Atacama Desert (**Figure 3c**) the equilibrium temperature of the ideal BE ($T_{\text{eq,BE}} = 1.3$ °C) is even lower than that of the ideal SE ($T_{\text{eq,SE}} = 1.5$ °C), and the T_{eq} values are ~14 °C lower than the ambient temperature ($T_{\text{amb}} = 15.4$ °C).

In this region, the ideal BE is almost always better than the ideal SE because, in dry conditions, the atmosphere is also partially transparent at wavelengths of 17–25 μm (**Figure 1b**), creating an additional cooling channel (29). For the same reason, the maximum net cooling power of the ideal BE ($P_{\text{cool, BE}}$) in the sub-ambient range is significantly higher than in the other regions, reaching up to 149 W/m^2 as shown in **Figure 3e**. It is clear that arid regions are the most-suitable for passive radiative cooling and, indeed, even animals have evolved to make use of this cooling potential: in particular, silver ants in the Sahara Desert have high solar reflectance and high mid-infrared emissivity over a broad wavelength range (36). It is also worth considering a dual-band selective emitter with high emissivity in the 8–13 and 17–25 μm wavelength ranges and low emissivity everywhere else, which can have marginally better performance in arid regions compared to even the BE; see **Supplementary Note 4** for the comparison between the ideal BE and the ideal dual-band SE.

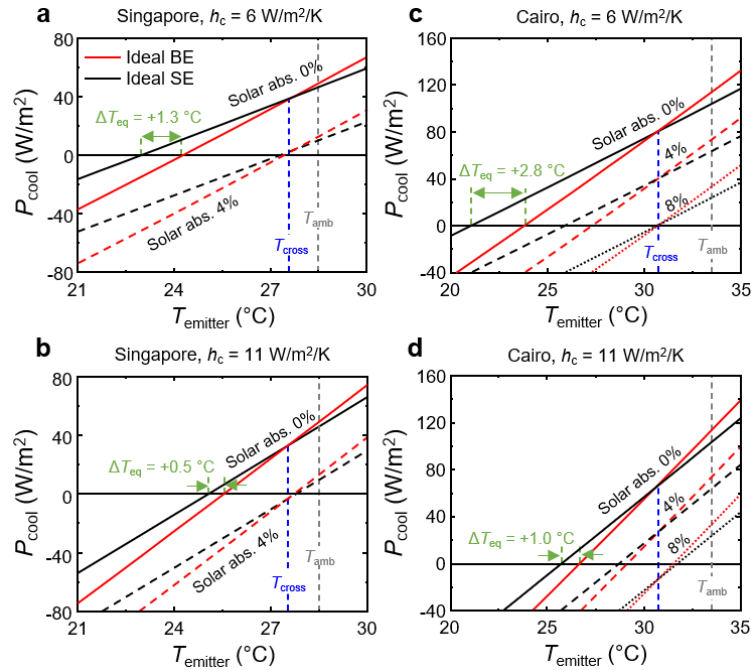


Figure 4. Cooling performance of the ideal BE and SE for different solar absorption, convection coefficient, and location (Singapore on May 1, 2023, and Cairo on Aug 1, 2023, at noon). **(a, b)** The net cooling power P_{cool} of the ideal BE (red line) and SE (black line), in Singapore, as a function of the emitter temperature (T_{emitter}) at **(a)** $h_c = 6 \text{ W}/\text{m}^2/\text{K}$ and **(b)** $h_c = 11 \text{ W}/\text{m}^2/\text{K}$. **(c, d)** The same graph but in Cairo at **(c)** $h_c = 6 \text{ W}/\text{m}^2/\text{K}$ and **(d)** $h_c = 11 \text{ W}/\text{m}^2/\text{K}$. The solar irradiance in Singapore on this day at noon was around $900 \text{ W}/\text{m}^2$ and that in Cairo was around $1000 \text{ W}/\text{m}^2$ (**Supplementary Note 2**).

To account for actual scenarios, we consider the effects of solar absorption and heat exchange through conduction and convection to air, in Singapore and Cairo. Singapore and Cairo were

selected because they are the least-suitable (Singapore) and most-suitable (Cairo) regions for the ideal SE compared to the ideal BE out of the locations we considered. **Figures 4a** and **4b** shows the net cooling power (P_{cool}) of the ideal BE and SE as a function of the emitter temperature (T_{emitter}) in Singapore for different h_c (6 and 11 W/m²/K). The solid lines represent no solar absorption, and the dashed lines represent the solar absorption of 4%, which corresponds to 36 W/m² (solar irradiance was 900 W/m² in Singapore on May 1st, 2023, at noon and see **Supplementary Note 2**). Here, we use two metrics to compare the ideal BE and SE: the difference in the equilibrium temperature of the ideal BE and SE, $\Delta T_{\text{eq}} = T_{\text{eq, BE}} - T_{\text{eq, SE}}$, and the net cooling power (P_{cool}) at T_{cross} (**Figure 4a**). P_{cool} at T_{cross} is the maximum power where the ideal SE can outperform the ideal BE. Even without solar absorption, ΔT_{eq} in Singapore is only 0.5–1.3 °C and P_{cool} at T_{cross} (27.5 °C) is only 32–38 W/m² in the practical h_c range of 6–11 W/m²/K. Both ΔT_{eq} and P_{cool} (at T_{cross}) decrease with increasing h_c because conduction and convection hinder cooling more significantly as the $T_{\text{amb}} - T_{\text{emitter}}$ increases. For solar absorption of 4%, both emitters show almost the same cooling ability in the sub-ambient range, and their cooling performance is poor on both metrics. Accordingly, in this region, minimizing solar absorption is more important than whether the emissivity in the mid-IR range is broad or selective.

Figures 4c and **4d** show the net cooling power of the ideal BE (red) and SE (black lines) in Cairo as a function of T_{emitter} for different h_c . The maximum ΔT_{eq} without solar absorption is limited to 1.0–2.8 °C; note that ΔT_{eq} values were obtained by assuming no thermal load on the ideal emitters, but in actual scenarios, where thermal load is connected to the emitters, the actual ΔT_{eq} values should be lower than the calculated ones. Even without solar absorption, P_{cool} at T_{cross} (= 30.6 °C) is limited to 65–79 W/m² in the practical h_c range. When considering that a practical operational temperature range may be within a few degrees from the ambient temperature (T_{amb}) (6, 7), it is difficult to say that the ideal SE is meaningfully better than the ideal BE for sub-ambient cooling even in this region where the SE should be most-beneficial compared to the BE.

Finally, we also consider *actual* emitters in practical scenarios: Singapore (May 1st, 2023) and Cairo (Aug 1st, 2023) with $h_c = 6$ W/m²/K. The absorption/emission spectra of a total of 16 experimentally demonstrated emitters were extracted from the literature: 8 actual BEs (3, 5, 26, 30, 37-40) (red circles) and 8 actual SEs (1, 7, 14, 21, 25, 41-43) (black circles). See **Figures 5c,d** and **Supplementary Note 5** for the absorption/emission spectra of the actual emitters from literature, where we had to make some minor extrapolations in wavelength ranges where data was

not available (the dotted line). **Figure 5a** shows the equilibrium temperature of the actual BEs (red symbols) and SEs (black symbols), and that of the ideal BE (red line) and SE (black line) in Singapore as a function of solar absorption, and **Figure 5b** shows the same plot in Cairo. Interestingly, T_{eq} of the most actual BEs (red circles) are close to those of the ideal BE (red line), while T_{eq} of the actual SEs (black circles) are relatively far from those of the ideal SE (black line); this is an indication that an ideal-BE-like emitter is easier to fabricate and has been realized many times, while the design and fabrication of an ideal-SE-like emitter remains a challenge. Note also that T_{eq} values of the actual SEs (black symbols) in Singapore (**Figure 5a**) are closer to T_{eq} of the ideal SE (black line) than those in Cairo (**Figure 5b**). This implies that minimizing solar absorption is more important than whether the emissivity in the mid-IR range is broad or selective in Singapore. Moreover, the actual BEs tend to have less solar absorption than the actual SEs, indicating that it remains a challenge to simultaneously achieve selective thermal emissivity and low solar absorption. We need to consider whether it is worth the significant extra effort to design and fabricate close-to-ideal SEs to obtain (at best) minor improvement in performance compared to BEs.

In practice, outdoor radiative cooling has another limitation: dust accumulation on an emitter can significantly affect the cooling potential because of increased solar absorption. A recent study experimentally showed that the net cooling power (P_{cool}) during the daytime was reduced by 6–7 W/m² for every 1 g/m² of dust deposited on an emitter (44). Meanwhile, one experiment reported an accumulation of 10.3 g/m² of dust on an outdoor 15° tilted solar panel after 70 days, from May to August in Iran in 2016 (45). Taking these two examples together, we can estimate that a radiative-cooling panel would pick up an additional 6–7% of solar absorption, corresponding to 60–70 W/m². Thus, we suggest that radiative-cooling surfaces that minimize dust accumulation or enable easy cleaning should be a design goal as well, perhaps using super-hydrophobic surfaces or similar strategies (46, 47).

Note that the present paper specifically considers radiative-cooling surfaces that face the sky. The analysis may be somewhat different in the case of vertically oriented cooling surfaces, such as those on the walls of buildings or on textiles, where the emitter is exchanging radiation with both the sky and the ground, or other elements of the urban environment, and thus wavelength selectivity can help simultaneously to provide cooling toward the sky and limit heating from everywhere else (48).

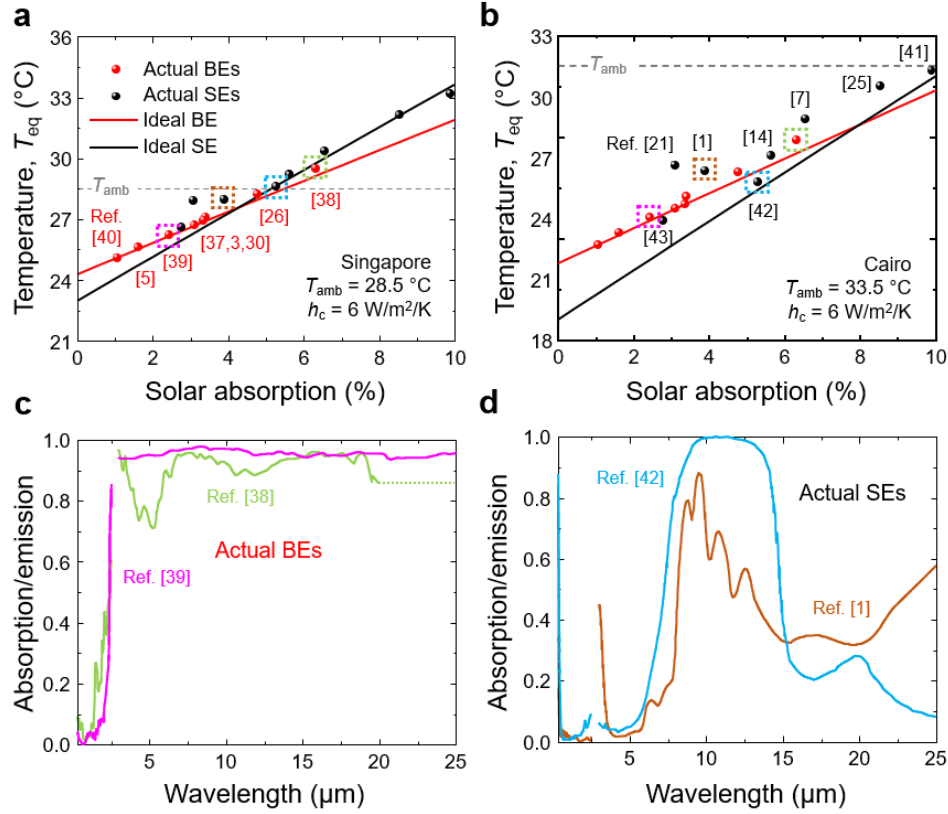


Figure 5. Calculated cooling performance of the ideal and actual BEs and SEs as a function of solar absorption. Here, “actual” means that the emissivity spectrum is taken from experiments in the literature [actual BEs(3, 5, 26, 30, 37-40) and SEs(1, 7, 14, 21, 25, 41-43)]. **(a, b)** The equilibrium temperature (T_{eq}) of the ideal emitters (lines) and the actual emitters (symbols) in **(a)** Singapore and **(b)** Cairo. h_c was set to $6 \text{ W/m}^2/\text{K}$. **(c, d)** The absorption/emission spectra ($0.3\text{--}2.5 \mu\text{m}$ and $3\text{--}25 \mu\text{m}$) of **(c)** actual BEs(38, 39) and **(d)** actual SEs(1, 42). The dotted line in (c) indicates extrapolations in wavelength ranges where data was not available. We observe that the actual $T_{eq, BE}$ values (red symbols) are mostly close to those of the ideal BE (red or blue line), while the values of the actual SEs (black symbols) are substantially above those of the ideal SE (black line), indicating that an ideal BE-like emitter is easier to design and fabricate. In addition, there are more actual BEs in the literature with low solar-absorption values.

It is meaningful to consider how much cooling power is available via passive radiative cooling compared to conventional active cooling driven by sunlight, for example an air conditioner powered by solar panels. The radiative cooling power of the ideal BE at ambient temperature is typically $50\text{--}100 \text{ W/m}^2$ (**Figure 3e**), and the cooling power over a day (24 h) is $1.2\text{--}2.4 \text{ kWh/m}^2/\text{day}$. For comparison, the cooling power of an air conditioner powered by solar panels is roughly $5 \text{ kWh/m}^2/\text{day}$, assuming 20% solar-panel efficiency and the efficiency of an air conditioner, which is the cooling power divided by the total electricity input, of more than 410% (see **Supplementary Note 6** for a detailed calculation). So, active cooling power using sunlight is expected to be 2–4 times higher than the radiative passive cooling power when averaged over the

entire 24-hour day, assuming the same area for solar panels as for radiative cooling surfaces. Of course, there are advantages to an all-passive cooling system with no moving parts, and both approaches can also work in tandem to maximize cooling potential. The value of radiative cooling can also be maximized when the cost of a radiative cooling system is significantly lower than that of the active cooling system. Since BE-like emitters are easier to realize than SEs (**Figures 5a, b**), they are likely to be less expensive as well.

Finally, we note that the atmospheric transmittance (τ_{atm}) spectra obtained from the NASA PSG with the MERRA-2 database does not directly incorporate the effects of real-time clouds and rain. Clouds can partially block sunlight, but also reduce τ_{atm} and therefore the capacity for radiative cooling. Depending on the degree of cloudiness and the type and thickness of clouds, they can block 0~90% of solar irradiance (49, 50), and 0~80% of τ_{atm} (51-53). In general, high-level clouds located above 6 km from sea level, such as cirrus and cirrostratus usually block 0~20% of solar irradiance (49, 50), and 0~20% of τ_{atm} (51). On the other hand, thick low-level clouds, such as stratus and nimbostratus, can reduce solar irradiance by as much as 80~90% (49, 50), and τ_{atm} by as much as 60~80% (52, 53). In addition, rain also significantly affects τ_{atm} (53), and the reduction of radiative cooling on a rainy day has been experimentally demonstrated (54).

In summary, we evaluated the cooling performance of ideal and realistic sky-facing broadband emitters (BEs) and selective emitters (SEs), for various locations on Earth. For emitter temperatures at or higher than the ambient temperature, broadband emitters always provide higher net cooling power, while for sub-ambient cooling, selective emitters are usually preferred but the difference in cooling power is small. Our calculations lead to the conclusion that large-scale deployment of sky-facing passive radiative cooling technologies should focus on design and manufacturing of scalable low-cost surfaces with the lowest possible solar absorption, but without worrying too much whether the emitter is broadband (*i.e.*, emissivity ~ 1 across the 3-25 μm range) or narrowband (*i.e.*, emissivity ~ 1 only in the 8-13 μm range).

Acknowledgements: This paper was supported in part by the NSF (1750341), DARPA (HR00112390123), and the UW-Madison VCR with funding from the Wisconsin Alumni Research Foundation (WARF). We thank Aaswath Raman and Jyotirmoy Mandal for critical reading of the first version of this manuscript, and their feedback.

Reference

1. A. P. Raman, M. A. Anoma, L. Zhu, E. Rephaeli, S. Fan, Passive radiative cooling below ambient air temperature under direct sunlight. *Nature* **515**, 540-544 (2014).
2. S. Fan, W. Li, Photonics and thermodynamics concepts in radiative cooling. *Nature Photonics* **16**, 182-190 (2022).
3. J. Mandal *et al.*, Hierarchically porous polymer coatings for highly efficient passive daytime radiative cooling. *Science* **362**, 315-319 (2018).
4. J. Mandal, Y. Yang, N. Yu, A. P. Raman, Paints as a scalable and effective radiative cooling technology for buildings. *Joule* **4**, 1350-1356 (2020).
5. X. Li, J. Peoples, P. Yao, X. Ruan, Ultrawhite BaSO₄ paints and films for remarkable daytime subambient radiative cooling. *ACS Applied Materials & Interfaces* **13**, 21733-21739 (2021).
6. E. A. Goldstein, A. P. Raman, S. Fan, Sub-ambient non-evaporative fluid cooling with the sky. *Nature Energy* **2**, 1-7 (2017).
7. D. Zhao *et al.*, Subambient cooling of water: toward real-world applications of daytime radiative cooling. *Joule* **3**, 111-123 (2019).
8. S. Zeng *et al.*, Hierarchical-morphology metafabric for scalable passive daytime radiative cooling. *Science* **373**, 692-696 (2021).
9. B. Zhu *et al.*, Subambient daytime radiative cooling textile based on nanoprocessed silk. *Nature Nanotechnology* **16**, 1342-1348 (2021).
10. L. Zhu, A. Raman, K. X. Wang, M. Abou Anoma, S. Fan, Radiative cooling of solar cells. *Optica* **1**, 32-38 (2014).
11. W. Li, Y. Shi, K. Chen, L. Zhu, S. Fan, A comprehensive photonic approach for solar cell cooling. *ACS Photonics* **4**, 774-782 (2017).
12. K. W. Lee *et al.*, Visibly clear radiative cooling metamaterials for enhanced thermal management in solar cells and windows. *Advanced Functional Materials* **32**, 2105882 (2022).
13. M. Zhou *et al.*, Vapor condensation with daytime radiative cooling. *Proceedings of the National Academy of Sciences* **118**, e2019292118 (2021).
14. D. Chae, S. Son, Y. Liu, H. Lim, H. Lee, High-performance daytime radiative cooler and near-ideal selective emitter enabled by transparent sapphire substrate. *Advanced Science* **7**, 2001577 (2020).
15. J. Fei *et al.*, Switchable surface coating for bifunctional passive radiative cooling and solar heating. *Advanced Functional Materials* **32**, 2203582 (2022).
16. G. Qi *et al.*, Ordered-porous-array polymethyl methacrylate films for radiative cooling. *ACS Applied Materials & Interfaces* **14**, 31277-31284 (2022).
17. Y. Zhu *et al.*, Color-preserving passive radiative cooling for an actively temperature-regulated enclosure. *Light: Science & Applications* **11**, 122 (2022).
18. M. Li *et al.*, A UV-Reflective Organic-Inorganic Tandem Structure for Efficient and Durable Daytime Radiative Cooling in Harsh Climates. *Small* **19**, 2301159 (2023).
19. X. Meng, Z. Chen, C. Qian, Q. Li, X. Chen, Durable and mechanically robust superhydrophobic radiative cooling coating. *Chemical Engineering Journal* **478**, 147341 (2023).
20. T. Wang *et al.*, Bioinspired Switchable Passive Daytime Radiative Cooling Coatings. *ACS Applied Materials and Interfaces* **15**, 48716-48724 (2023).
21. D. Li *et al.*, Scalable and hierarchically designed polymer film as a selective thermal emitter for high-performance all-day radiative cooling. *Nature Nanotechnology* **16**, 153-158 (2021).
22. B. Zhao *et al.*, Considerations of passive radiative cooling. *Renewable Energy* **219**, 119486 (2023).
23. Gemini Observatory, <https://www.gemini.edu/observing/telescopes-and-sites/sites#Transmission>. (accessed Mar-19-2024).

24. J.-I. Kou, Z. Jurado, Z. Chen, S. Fan, A. J. Minnich, Daytime radiative cooling using near-black infrared emitters. *ACS Photonics* **4**, 626-630 (2017).
25. S.-Y. Heo *et al.*, A Janus emitter for passive heat release from enclosures. *Science Advances* **6**, eabb1906 (2020).
26. X. Li *et al.*, Full daytime sub-ambient radiative cooling in commercial-like paints with high figure of merit. *Cell Reports Physical Science* **1** (2020).
27. Y. Jin, Y. Jeong, K. Yu, Infrared-Reflective Transparent Hyperbolic Metamaterials for Use in Radiative Cooling Windows. *Advanced Functional Materials* **33**, 2207940 (2023).
28. C. Chen *et al.*, Manipulating Hetero-nanowire Films for Flexible and Multifunctional Thermoelectric Devices. *Advanced Materials*, 2400020 (2024).
29. X. Wu *et al.*, A dual-selective thermal emitter with enhanced subambient radiative cooling performance. *Nature Communications* **15**, 815 (2024).
30. B. Xiang *et al.*, 3D porous polymer film with designed pore architecture and auto-deposited SiO₂ for highly efficient passive radiative cooling. *Nano Energy* **81**, 105600 (2021).
31. R. W. Bliss Jr, Atmospheric radiation near the surface of the ground: a summary for engineers. *Solar Energy* **5**, 103-120 (1961).
32. The NASA Planetary Spectrum Generator, <https://psg.gsfc.nasa.gov/>. (accessed 18 December 2023).
33. R. Gelaro *et al.*, The modern-era retrospective analysis for research and applications, version 2 (MERRA-2). *Journal of Climate* **30**, 5419-5454 (2017).
34. J. Mandal, X. Huang, A. P. Raman, Accurately Quantifying Clear-Sky Radiative Cooling Potentials: A Temperature Correction to the Transmittance-Based Approximation. *Atmosphere* **12**, 1195 (2021).
35. F. Fan, D. Xu, Y. Zhu, G. Tan, D. Zhao, A simple, accurate, and universal method for characterizing and comparing radiative cooling materials and devices. *International Journal of Heat and Mass Transfer* **200**, 123494 (2023).
36. N. N. Shi *et al.*, Keeping cool: Enhanced optical reflection and radiative heat dissipation in Saharan silver ants. *Science* **349**, 298-301 (2015).
37. S. Jeong, C. Y. Tso, Y. M. Wong, C. Y. Chao, B. Huang, Daytime passive radiative cooling by ultra emissive bio-inspired polymeric surface. *Solar Energy Materials & Solar Cells* **206**, 110296 (2020).
38. Y. Tian *et al.*, Superhydrophobic and recyclable cellulose-fiber-based composites for high-efficiency passive radiative cooling. *ACS Applied Materials & Interfaces* **13**, 22521-22530 (2021).
39. X. Song, Y. Gao, P. Zhang, A bioinspired and scalable near-ideal broadband coating for radiative thermoregulation. *Journal of Materials Chemistry A* **10**, 22166-22174 (2022).
40. Y. C. A. Tsang, N. J. Varghese, M. Degeorges, J. Mandal, Porous polymer bilayer with near-ideal solar reflectance and longwave infrared emittance. *Nanophotonics* **13**, 669-677 (2024).
41. H. Bao *et al.*, Double-layer nanoparticle-based coatings for efficient terrestrial radiative cooling. *Solar Energy Materials and Solar Cells* **168**, 78-84 (2017).
42. Y. Yang *et al.*, Bulk material based selective infrared emitter for sub-ambient daytime radiative cooling. *Solar Energy Materials and Solar Cells* **211**, 110548 (2020).
43. U. Banik *et al.*, Efficient thin polymer coating as a selective thermal emitter for passive daytime radiative cooling. *ACS Applied Materials and Interfaces* **13**, 24130-24137 (2021).
44. F. Fan, Q. Xu, D. Zhao, Heat transfer properties of dusty radiative cooling surface: Modeling and experimental studies. *International Journal of Heat and Mass Transfer* **214**, 124465 (2023).
45. A. Gholami, A. Saboonchi, A. A. Alemrajabi, Experimental study of factors affecting dust accumulation and their effects on the transmission coefficient of glass for solar applications. *Renewable energy* **112**, 466-473 (2017).

46. G. Chen *et al.*, A visibly transparent radiative cooling film with self-cleaning function produced by solution processing. *Journal of Materials Science and Technology* **90**, 76-84 (2021).
47. J. Song, Q. Shen, H. Shao, X. Deng, Anti-Environmental Aging Passive Daytime Radiative Cooling. *Advanced Science* **11**, 2305664 (2024).
48. J. Mandal, S. Mandal, J. Brewer, A. Ramachandran, A. P. Raman, Radiative cooling and thermoregulation in the earth's glow. *arXiv:2006. 11931* (2020).
49. E. Vowinckel, S. Orvig, Relation between Solar Radiation Income and Cloud Type in the Arctic. *Journal of Applied Meteorology Climatology* **1**, 552-559 (1962).
50. D. Matuszko, Influence of the extent and genera of cloud cover on solar radiation intensity. *International Journal of Climatology* **32**, 2403-2414 (2012).
51. D. M. Gates, C. C. Shaw, Infrared Transmission of Clouds. *Journal of the Optical Society of America* **50**, 876-882 (1960).
52. P. Kuhn, H. Weickmann, M. Lojko, L. Stearns, Transfer of Infrared Radiation Through Clouds. *Applied Optics* **13**, 512-517 (1974).
53. C. C. Chen (1975) Attenuation of electromagnetic radiation by haze, fog, clouds, and rain. (<https://apps.dtic.mil/sti/citations/tr/ADA011642>).
54. Y. Gao, X. Song, A. S. Farooq, P. Zhang, Cooling performance of porous polymer radiative coating under different environmental conditions throughout all-year. *Solar Energy* **228**, 474-485 (2021).

Supporting Information

For sky-facing passive radiative cooling, are wavelength-selective emitters the best choice?

Yeonghoon Jin¹ and Mikhail Kats^{1,2}*

¹Department of Electrical and Computer Engineering, University of Wisconsin-Madison, Madison, WI, USA

²Department of Material Science and Engineering, University of Wisconsin-Madison, Madison, WI, USA

E-mail: mkats@wisc.edu

Supplementary Note 1. Net spectral radiative cooling power of the ideal BE and SE

Cairo (Aug 1st, 2023)
 $T_{\text{amb}} = 33.5 \text{ }^\circ\text{C}$

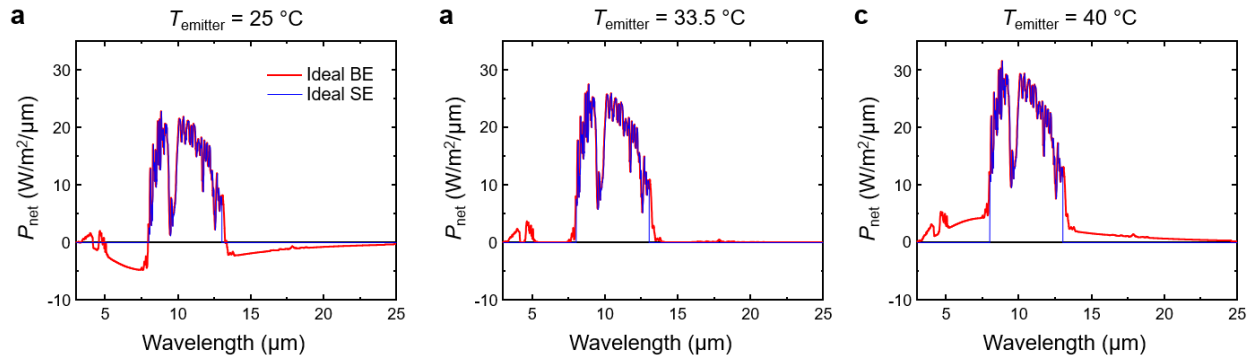


Figure S1. Net spectral radiative cooling power (P_{net}) of the ideal BE and SE in Cairo on Aug 1, 2023, at noon, which is given by $P_{\text{net}} = P_{\text{rad}} - P_{\text{atm}}$, where P_{rad} is the power radiated from an emitter, and P_{atm} is the power radiated from the atmosphere and then absorbed by the emitter. See **Supplementary Note 3** for detailed calculation. The ambient temperature (T_{amb}) on the same day was $33.5 \text{ }^\circ\text{C}$ and the emitter temperature (T_{emitter}) is assumed to be (a) $25 \text{ }^\circ\text{C}$, (b) $33.5 \text{ }^\circ\text{C}$, and (c) $40 \text{ }^\circ\text{C}$. When T_{emitter} is $25 \text{ }^\circ\text{C}$, the wavelengths outside the atmospheric window ($8\text{--}13 \mu\text{m}$) mainly serve as the heating channel (red line) and thus the ideal SE (blue) shows higher P_{net} values, while those serve as the cooling channel when T_{emitter} is $40 \text{ }^\circ\text{C}$.

Supplementary Note 2. How to use the NASA PSG

[1] Obtaining atmospheric information using the PSG

Atmospheric transmittance (τ_{atm}) can be accessed through the PSG (1, 2). The following is an example for obtaining atmospheric temperature and gas composition and partial atmospheric emissivity in Singapore on May 1st, 2023 at noon.

1) Go to the PSG website (<https://psg.gsfc.nasa.gov/>) and load the template of “Earth Transmittance”.



2) Choose the “Change Object” section

- Change the date to “2023/05/01 04:00” because the time zone of Singapore is UTC (coordinated Universal Time) + 8. Click “Ephemeris” and then the geometrical properties will be automatically changed. We summarized the longitude/latitude and time zone of the selected five locations in **Table S1**.

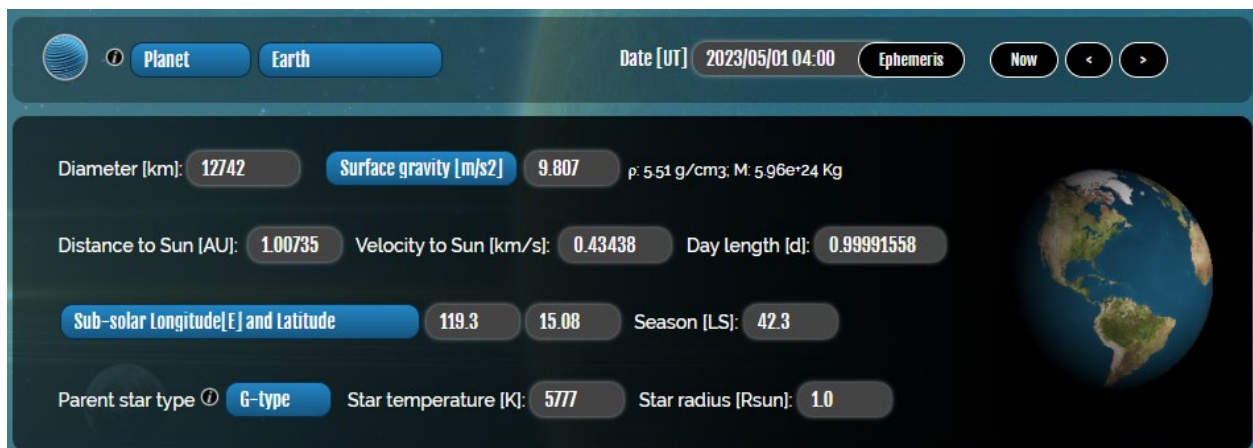
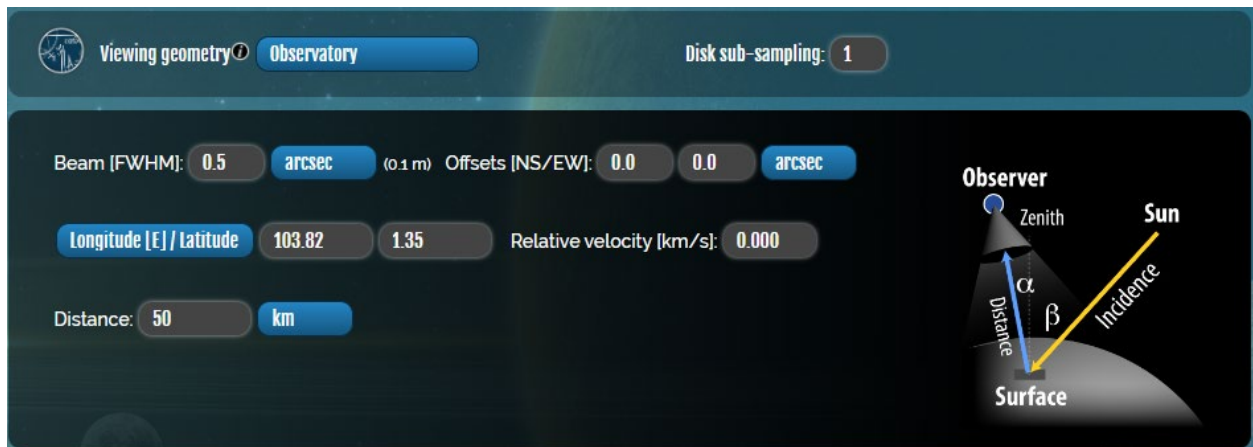


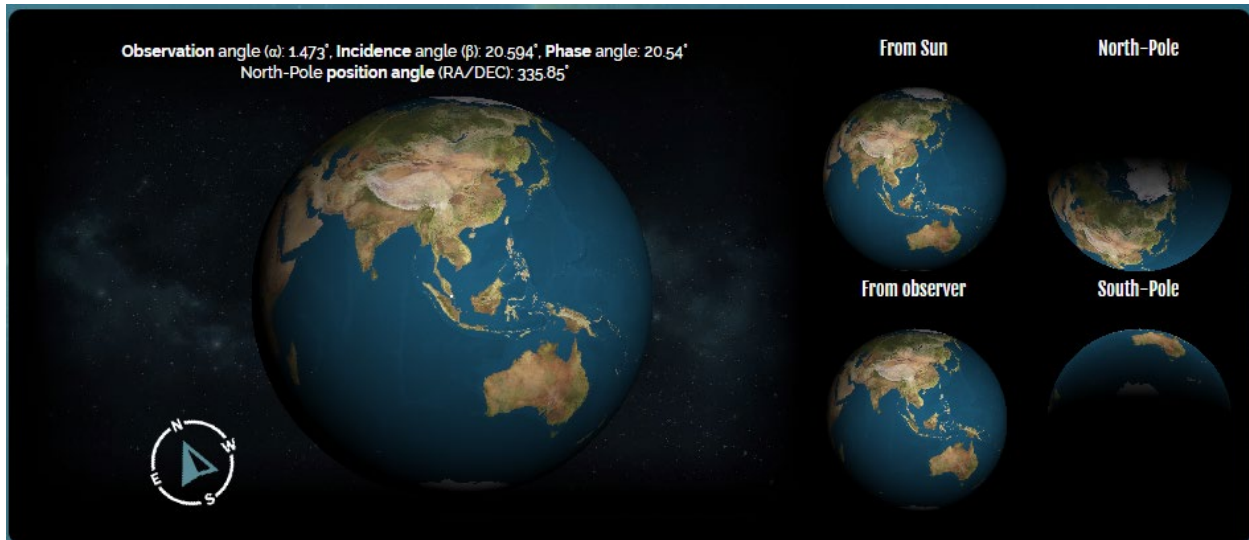
Table S1. Location and time information of the five regions.

Regions	Longitude/Latitude	Time zone	Time
Singapore	103.82°E/1.35°N	UTC + 8	May 1, 2023, at 12 pm
Houston, USA	264.63°E/29.76°N	UTC – 5	Aug 1, 2023, at 12 pm
Phoenix, USA	247.93°E/33.45°N	UTC – 7	Aug 1, 2023, at 12 pm
Cairo, Egypt	31.24°E/30.04°N	UTC + 2	Aug 1, 2023, at 12 pm
Atacama Desert, Chile	69.13°W/23.86°S	UTC – 4	Dec 1, 2023, at 12 pm

- Select the viewing geometry as “Observatory” and enter the longitude/latitude of Singapore (103.82°E/1.35°N, **Table S1**). The “Distance” is the distance between the Earth’s surface and the observer as depicted in the figure below, and we entered 50 km in this case. Here, the observer angle (α), which is the angle between the observer and the Earth zenith, is fixed to 1.473° in the PSG, so the “distance” is the pseudo-altitude. Note that the atmospheric transmittance (τ_{atm}) at a distance of 50 km is almost saturated, as described in the main text. The spatial domain of the data collecting area on the ground can be adjusted by the “Beam [FWHM]”, which is a circle in this case with a diameter defined by its Full-With-Half-Maximum, and we set this to the default of 0.5 arcsec (2.4×10^{-6} radian), which corresponds to 0.12 m. The Disk sub-sampling was also set to a default value of 1. Refer to the reference (2) for detailed explanation of each parameter.

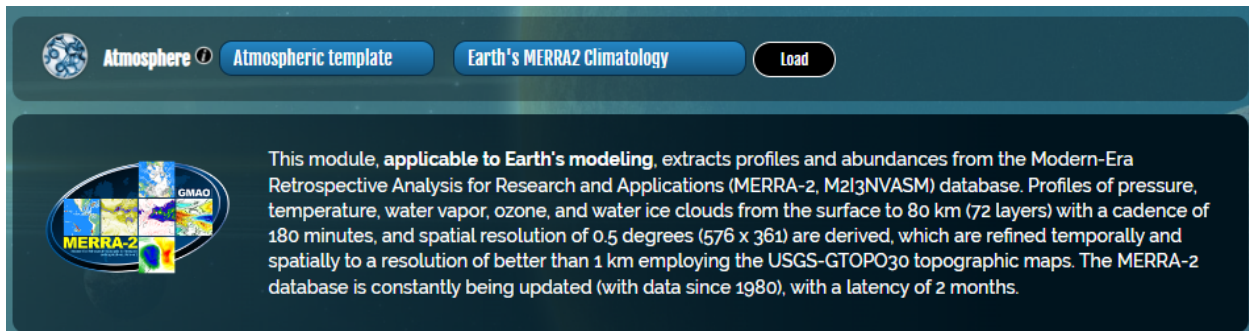


- Click the “Save settings” below and click the “Change Object” again. Then, one can observe a three-dimensional view of Earth as shown below. The target location is also indicated by a small white point. The observer angle α is 1.473° and the zenith angle of incidence of the sun β is 20.594° .

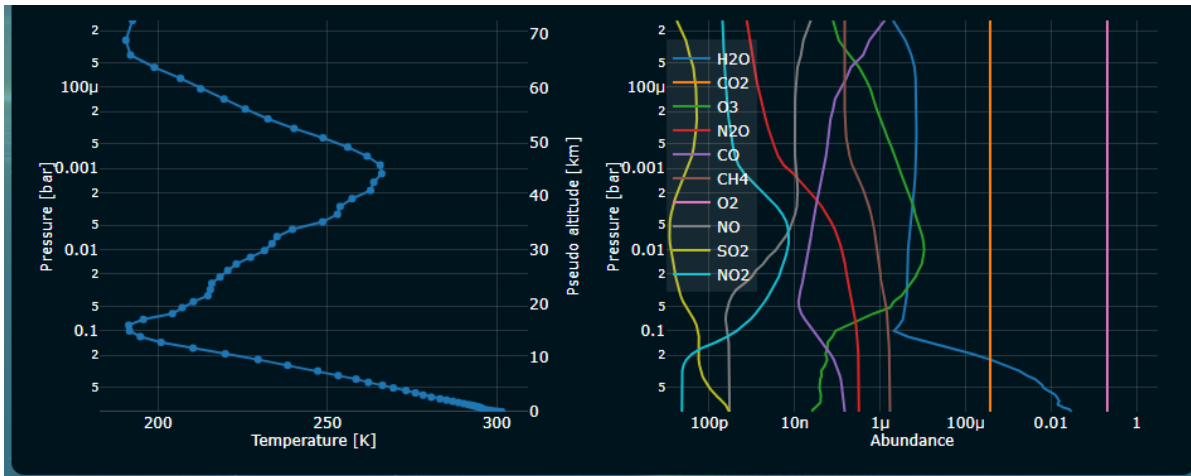


3) Choose the “Change Composition” section

- We chose an atmosphere extracted from MERRA-2 database by selecting “Earth’s MERRA2 Climatology” in “Atmospheric template”. The system automatically extracts the atmospheric temperature and gas composition for the location and time we entered.

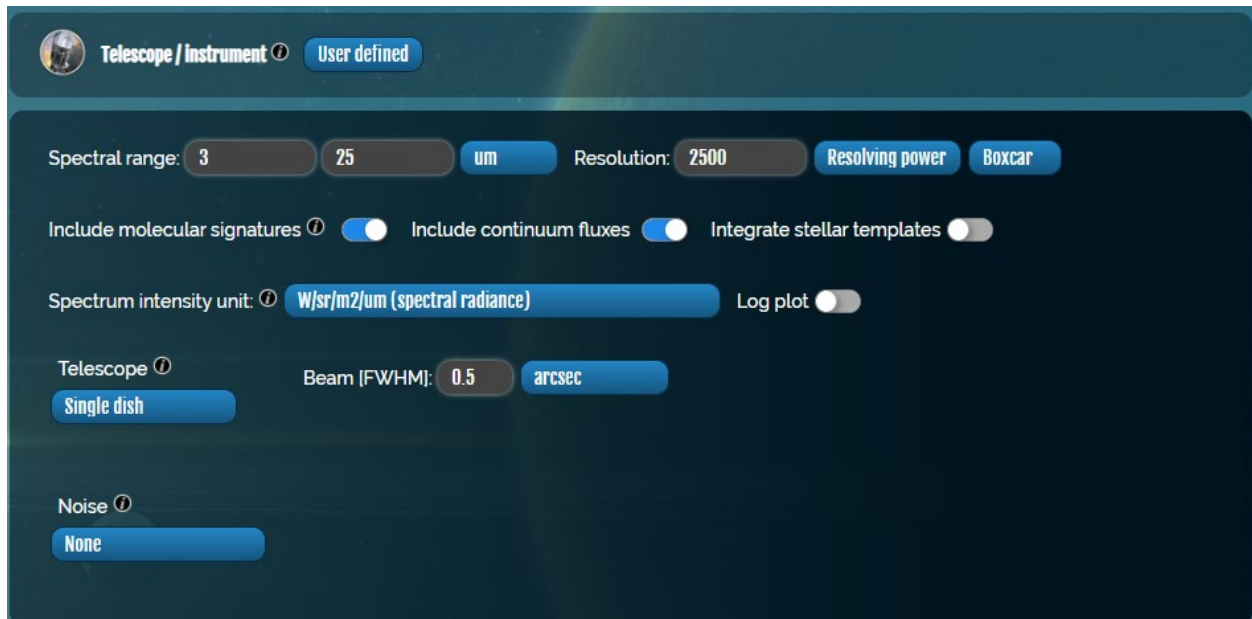


- The figure below shows the atmospheric temperature (left) and gas (right) profiles of Singapore on May 1, 2023 at noon. The gas abundance indicates the gas ratio with respect to the total pressure at a specific altitude. This means that the density of gases decreases with increasing altitude although the abundance is constant (such as CO_2 and O_2). The atmospheric temperature at a specific altitude can be extracted from this information.

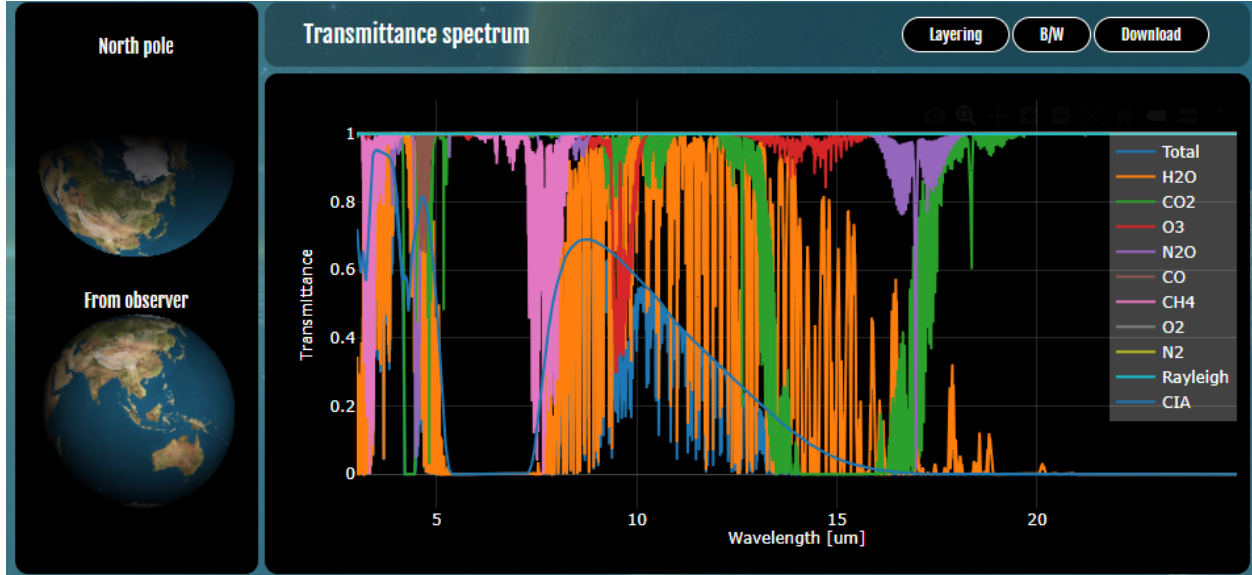


4) Choose the “Change Instrument” section

- “User defined” was chosen and we used the following information: the spectral range between 3 to 25 μm and the resolution of 2500 to obtain spectral radiance ($\text{W}/\text{sr}/\text{m}^2/\mu\text{m}$). The others were left as default as shown below.



- Click “Generate Spectra”. The atmospheric transmittance (τ_{atm}) and the contributions by atmospheric gases can be obtained. Click “Download” to get the spectra.



5) Obtaining altitude-dependent partial ε_{atm}

- Repeat the overall process by changing the “Distance” in the second step. In our case, we divided the atmosphere into 14 layers from 0~50 km above the ground and the layer information is shown in **Table S2**. For example, τ_{atm}^1 is the atmospheric transmittance from the bottom-most layer (0~0.5 km above the ground), and τ_{atm}^{14} is the atmospheric transmittance from 0~50 km above the ground. The corresponding atmospheric emissivities are $\varepsilon_{\text{atm}}^1$ and $\varepsilon_{\text{atm}}^{14}$ because $\varepsilon_{\text{atm}} = 1 - \tau_{\text{atm}}$.
- Partial ε_{atm} of the first atmospheric layer (0~0.5 km) is $\varepsilon_{\text{atm}}^1$. Partial ε_{atm} of the second atmospheric layer (0.5~1 km) is given by $\varepsilon_{\text{atm}}^2 - \varepsilon_{\text{atm}}^1$, and that of the third layer (1~1.5 km) is given by $\varepsilon_{\text{atm}}^3 - \varepsilon_{\text{atm}}^2$. In the same way, the partial ε_{atm} of i^{th} atmospheric layer is given by $\varepsilon_{\text{atm}}^i - \varepsilon_{\text{atm}}^{i-1}$, where $i = 2, 3, 4, \dots, 14$.

Table S2. Atmospheric temperature $T_{\text{atmosphere}}$ of each atmospheric layer at five locations on Earth. The atmospheric temperature of each layer up to the bottom 8 layers is the temperature at the lower altitude boundary, and that of the rest layers is the temperature at the center altitude.

Atmosphere layer	Singapore	Houston	Phoenix	Cairo	Atacama
0~0.5 km (1 st)	301.5 K	304.5 K	308.5 K	306.5 K	288.4 K
0.5~1.0 km	296.0 K	299.0 K	303.0 K	300.0 K	282.5 K
1.0~1.5 km	294.0 K	295.8 K	296.0 K	293.0 K	280.8 K
1.5~2.0 km	290.0 K	290.8 K	290.0 K	287.3 K	276.5 K
2.0~2.5 km	287.0 K	286.0 K	285.6 K	287.0 K	272.2 K
2.5~3.0 km	282.0 K	281.2 K	281.0 K	285.7 K	268.1 K
3.0~4.0 km	279.0 K	277.3 K	276.7 K	282.0 K	264.2 K
4.0~5.0 km	273.0 K	272.6 K	267.0 K	273.7 K	257.0 K
5.0~10 km	247.0 K	246.5 K	242.5 K	250.0 K	227.0 K
10~15 km	205.0 K	207.4 K	208.2 K	210.8 K	199.2 K
15~20 km	200.0 K	207.5 K	205.7 K	202.6 K	208.4 K
20~25 km	215.0 K	218.3 K	218.8 K	218.8 K	220.4 K
25~30 km	225.0 K	224.6 K	225.5 K	223.4 K	228.0 K
30~50 km	260.0 K	248.5 K	252.0 K	250.7 K	257.0 K

[2] Validation of τ_{atm} obtained from the PSG: τ_{atm} at Mauna Kea

To confirm the accuracy of atmospheric transmittance (τ_{atm}) obtained from the PSG, we compared τ_{atm} obtained from the Gemini Observatory (Mauna Kea, air mass 1.5, water vapor 1.6 mm) (3) to that obtained from the PSG (**Figure S2**). The longitude/latitude of 155.47°W/19.82°N (Mauna Kea) and three different times (May 1st, 2023, Aug 1st, 2023, and Dec 1st, 2023, always at noon) were used. The time zone of Mauna Kea is UTC−10. Both τ_{atm} show quite good agreement, and they show high τ_{atm} at the 17–25 μm wavelength range because of the high altitude (>4 km) of the Gemini Observatory.

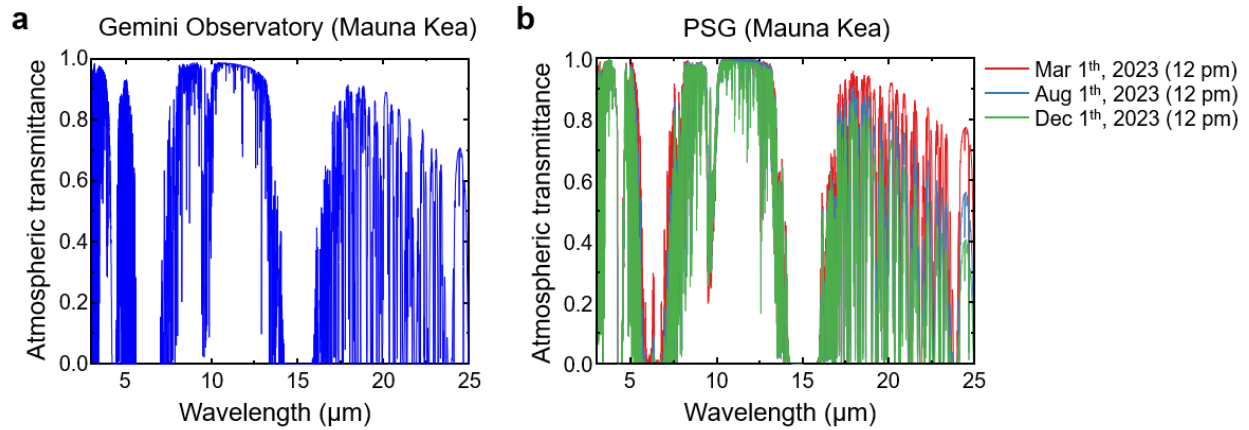


Figure S2. (a,b) τ_{atm} at the Gemini Observatory (Mauna Kea) obtained from (a) the Gemini Observatory and (b) the PSG.

[3] Obtaining solar irradiance using the PSG

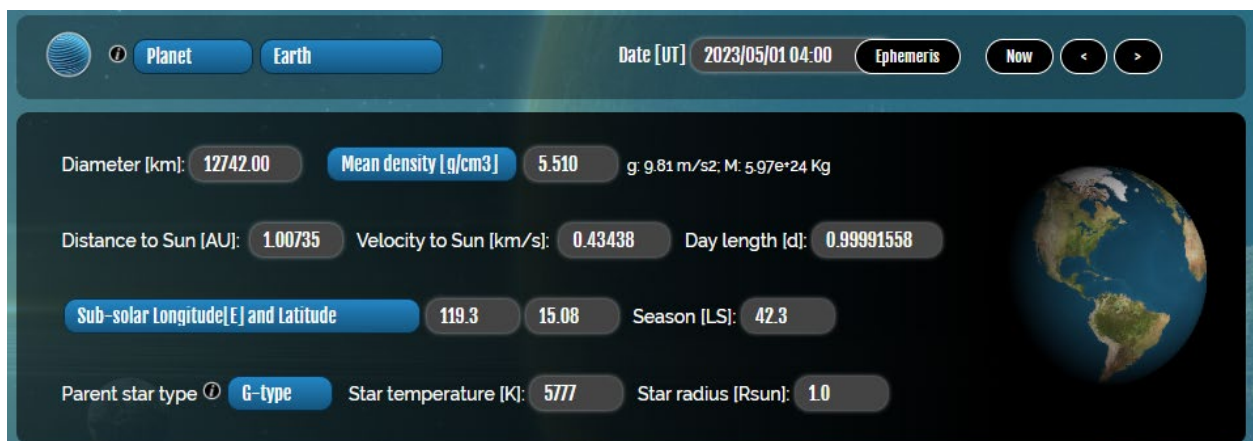
Solar irradiance for a specific location and time can be obtained through the NASA PSG. The following is an example for obtaining the solar irradiance spectrum in Singapore on May 1st, 2023 at noon.

1) Go to the PSG website (<https://psg.gsfc.nasa.gov/>) and load the template of “Sun from Earth”.

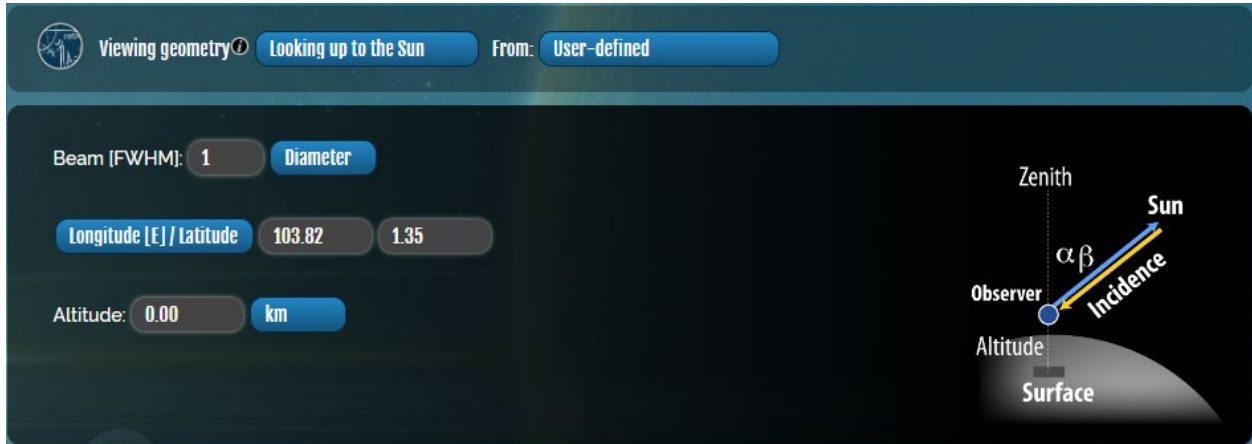


2) Choose the “Change Object” section

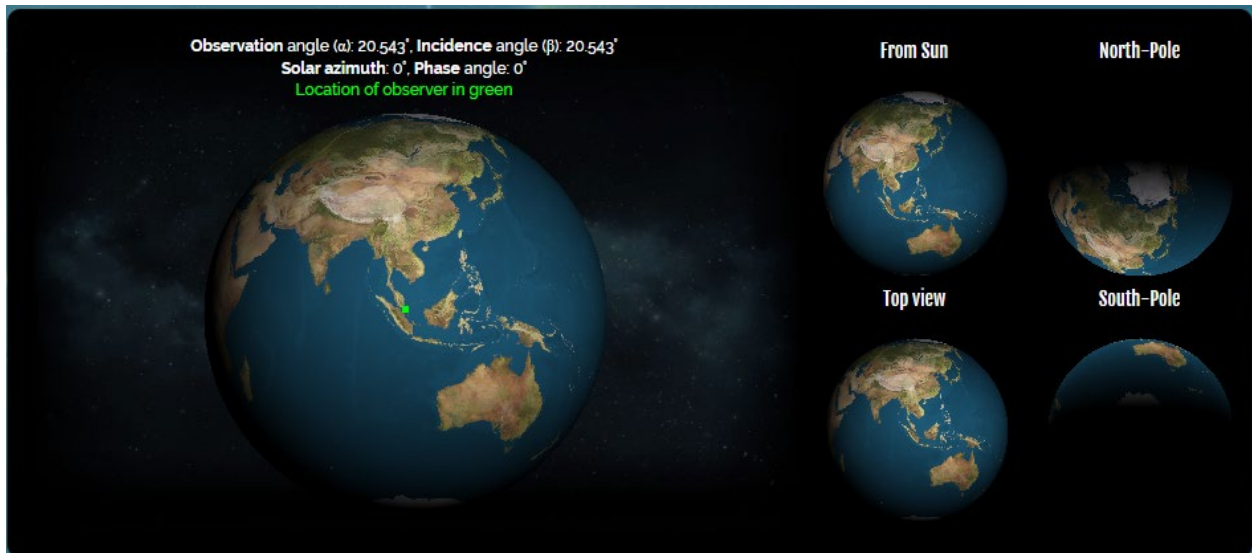
- Change the date to “2023/05/01 04:00” because the time zone of Singapore is UTC (coordinated Universal Time) + 8. Click “Ephemeris” and then the geometrical properties will be automatically changed. We also summarized the longitude/latitude and time zone of the selected five locations in above **Table S1**.



- Select the viewing geometry as “Looking up to the Sun” and enter the longitude/latitude of Singapore (103.82°E/1.35°N). The “Altitude” was set to 0 because we assumed that a thermal emitter is placed near the ground. Click “Save settings”.

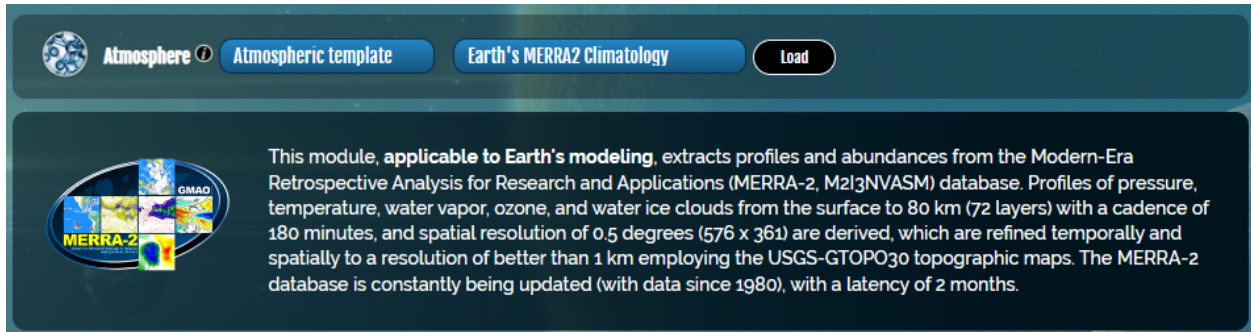


- Click the “Change Object” section again. Once the setting is complete, one can observe the location of the observer as shown below (green point). Here, the angle of incidence of solar energy (β) is automatically calculated and it is 20.543°.



3) Choose the “Change Composition” section

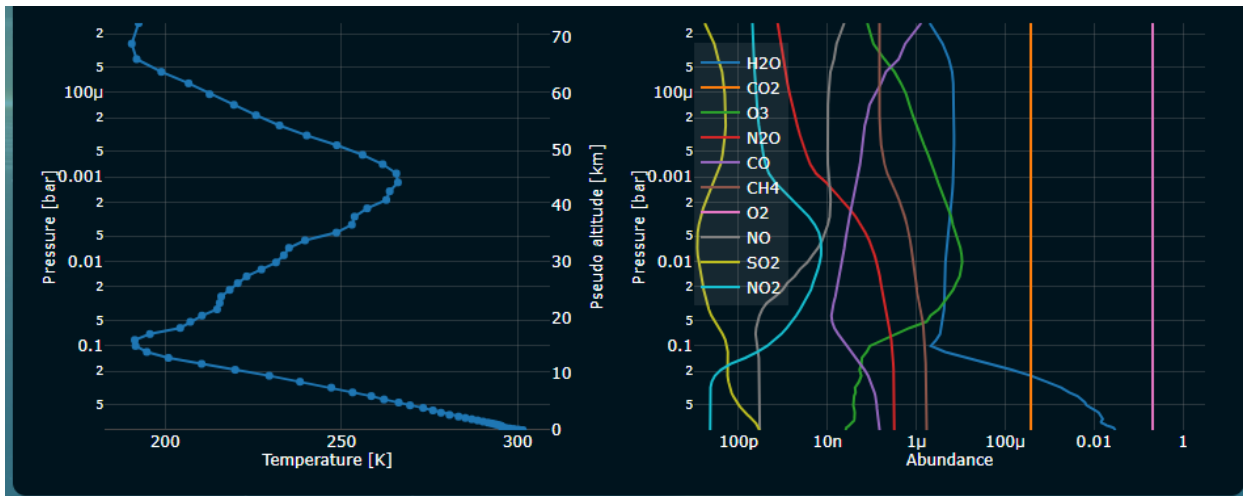
- We chose an atmosphere extracted from MERRA-2 database by selecting “Earth’s MERRA2 Climatology” in “Atmospheric template”. The system automatically extracts the atmospheric temperature and gas composition for the location and time we entered in the “Change Object” section.



The screenshot shows a software interface for selecting an atmospheric template. At the top, there are four buttons: "Atmosphere" (with a globe icon), "Atmospheric template", "Earth's MERRA2 Climatology" (highlighted in blue), and "Load". Below the buttons is a dark blue panel containing a MERRA-2 logo on the left and a text box on the right. The text box describes the module's applicability to Earth's modeling and details the data source (MERRA-2, M213NVASM), the variables extracted (pressure, temperature, water vapor, ozone, water ice clouds), the vertical range (0 to 80 km), the temporal cadence (180 minutes), and the spatial resolution (better than 1 km).

This module, **applicable to Earth's modeling**, extracts profiles and abundances from the Modern-Era Retrospective Analysis for Research and Applications (MERRA-2, M213NVASM) database. Profiles of pressure, temperature, water vapor, ozone, and water ice clouds from the surface to 80 km (72 layers) with a cadence of 180 minutes, and spatial resolution of 0.5 degrees (576 x 361) are derived, which are refined temporally and spatially to a resolution of better than 1 km employing the USGS-GTOPO30 topographic maps. The MERRA-2 database is constantly being updated (with data since 1980), with a latency of 2 months.

- Bottom figure shows the atmospheric temperature (left) and the atmospheric gas abundance (right) profiles of Singapore on May 1, 2023. The gas abundance indicates the ratio with respect to the total pressure at a specific altitude. This means that the density of gases decreases with increasing altitude although the abundance is constant (such as CO₂ and O₂).

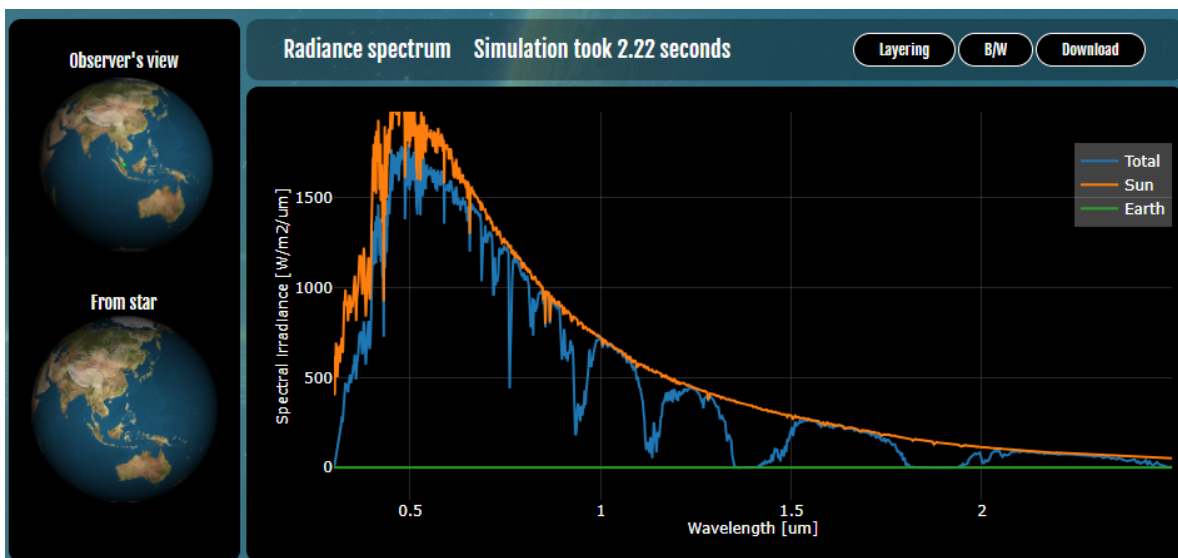


4) Choose the “Change Instrument” section

- “User defined” was chosen and we used the following input values: spectral range between 0.3 to 2.5 μm and resolution of 500. The others were left as default as shown below. Click “Save settings”.



- Click “Generate Spectra”. The solar spectrum that reaches the ground in Singapore is shown below (blue line). One can download the data.



- Before using data, we need to think about the surface normal direction of an emitter. The angle of incidence of solar energy with respect to the Earth zenith was 20.543° . If an emitter

is facing the sky that the surface normal direction is parallel to the Earth zenith, $\cos(20.543^\circ)$ should be multiplied to the integrated solar irradiance.

- The solar irradiance of Singapore (May 1, 2023, at noon) was around 900 W/m^2 , and that of Cairo (Aug 1, 2023, at noon) was around 1000 W/m^2 .

Supplementary Note 3. Calculation of P_{cool}

The calculation of the net cooling power per unit area (P_{cool}) is given by:(4)

$$P_{\text{cool}} = P_{\text{rad}}(T_{\text{emitter}}) - P_{\text{atm}}(T_{\text{atmosphere}}) - P_{\text{sun}} - P_{\text{con}}(T_{\text{emitter}}, T_{\text{amb}}), \quad (\text{S1})$$

where T_{emitter} is the temperature of an emitter, $T_{\text{atmosphere}}$ is the atmospheric temperature that varies with altitude as shown in **Figure 2a** in the main text, and T_{amb} is the ambient temperature (the temperature around the ground). $P_{\text{rad}}(T_{\text{emitter}})$, the power emitted from an emitter per unit area at T_{emitter} , is given by:

$$P_{\text{rad}}(T_{\text{emitter}}) = \int d\Omega \cos \theta \int_0^\infty d\lambda I_{\text{BB}}(T_{\text{emitter}}, \lambda) \varepsilon_{\text{emitter}}(\lambda, \theta), \quad (\text{S2})$$

where $d\Omega = 2\pi \int_0^{\pi/2} d\theta \sin \theta$, θ is the angle with respect to the surface normal direction, $I_{\text{BB}}(T_{\text{emitter}}, \lambda)$ is the spectral radiance of a blackbody at T_{emitter} , $\varepsilon_{\text{emitter}}(\lambda, \theta)$ is the emissivity of the emitter, and λ is the wavelength; we assumed that the emissivity of emitters was angle-independent, and thus $\varepsilon_{\text{emitter}}(\lambda, \theta=0^\circ)$ was used. $I_{\text{BB}}(T_{\text{emitter}}, \lambda) = \frac{2hc^2}{\lambda^5} \frac{1}{e^{hc/\lambda k_B T_{\text{emitter}}} - 1}$, where h is the Plank's constant, c is the speed of light, and k_B is the Boltzmann constant. The integration range of wavelengths was set to 3–25 μm , and it is very reasonable to consider this range (**Figure S3**). Atmospheric gases also emit thermal energy, and the emitter will absorb some of that energy. Here, we divided the atmosphere into 14 layers. The power emitted by the atmospheric gases depends on the atmospheric temperature ($T_{\text{atmosphere}}$), and the temperature varies with altitude (**Figure 2a** in the main text); $T_{\text{atmosphere}}$ of each layer is summarized in above **Table S2**. The power emitted by atmospheric gases and absorbed by an emitter (P_{atm}) is given by:

$$P_{\text{atm}} = \sum_{i=1}^n P_{\text{atm}}^i, \quad (\text{S3})$$

where P_{atm}^i is the power emitted from the i^{th} atmospheric layer and absorbed by the emitter, and n is the total number of the atmospheric layer ($n = 14$ in our case). P_{atm}^1 can be given by:

$$P_{\text{atm}}^1(T_{\text{atmosphere}}^1) = \int d\Omega \cos \theta \int_0^\infty d\lambda I_{\text{BB}}(T_{\text{atmosphere}}^1, \lambda) \varepsilon_{\text{emitter}}(\lambda, \theta) \varepsilon_{\text{atm}}^1(\lambda, \theta), \quad (\text{S4})$$

where $T_{\text{atmosphere}}^1$ is the atmospheric temperature of the 1st layer, and $\varepsilon_{\text{atm}}^1$ is the atmospheric emissivity of the 1st atmospheric layer (0~0.5 km above the ground). See **Supplementary Note 2** for how to obtain ε_{atm} . The integration range of wavelengths was set to 3–25 μm . From the 2nd to i^{th} atmospheric layer, P_{atm}^i can be given by:

$$P_{\text{atm}}^i(T_{\text{atmosphere}}^i) = \int d\Omega \cos \theta \int_0^\infty d\lambda I_{\text{BB}}(T_{\text{atmosphere}}^i, \lambda) \varepsilon_{\text{emitter}}(\lambda, \theta) [\varepsilon_{\text{atm}}^i(\lambda, \theta) - \varepsilon_{\text{atm}}^{i-1}(\lambda, \theta)], \quad (\text{S5})$$

where $T_{\text{atmosphere}}^i$ is the atmospheric temperature of i^{th} layer, and $\varepsilon_{\text{atm}}^i$ is the atmospheric emissivity from the ground to i^{th} layer. Note that **Equation S5** is different from the conventional calculation method with the uniform atmosphere assumption, which is given by: $P_{\text{atm}} = \int d\Omega \cos \theta \int_0^\infty d\lambda I_{\text{BB}}(T_{\text{amb}}, \lambda) \varepsilon_{\text{emitter}}(\lambda, \theta) \varepsilon_{\text{atm}}(\lambda, \theta)$, where the single ambient temperature value, T_{amb} , which corresponds to $T_{\text{atmosphere}}^1$ in this case, represents the entire atmospheric temperature, and the single ε_{atm} spectrum, which corresponds to $\varepsilon_{\text{atm}}^{14}$ in this case, is used. The power absorbed by the emitter from solar energy per unit area, P_{sun} , is given by:

$$P_{\text{sun}} = \int_0^\infty d\lambda \varepsilon_{\text{emitter}}(\lambda, \theta_{\text{sun}}) I_{\text{Solar}}(\lambda), \quad (\text{S6})$$

where I_{Solar} is the solar spectral irradiance of a specific region. See **Supplementary Note 2** for how to obtain I_{Solar} through the PSG. The non-radiative heat exchanged through conduction and convection per unit area, P_{con} , is given by:

$$P_{\text{con}} = h_c(T_{\text{amb}} - T_{\text{emitter}}), \quad (\text{S7})$$

where h_c is a heat transfer coefficient. **Figure S4** shows the cooling performance (the equilibrium temperature T_{eq} and the net cooling power P_{cool} at T_{amb}) of the ideal BE and SE in the five selected locations calculated by two different calculation methods: the uniform atmosphere and the gradient atmosphere. Because of the colder sky, the cooling performance calculated by the gradient atmosphere is somewhat better than that calculated by the conventional uniform atmosphere assumption.

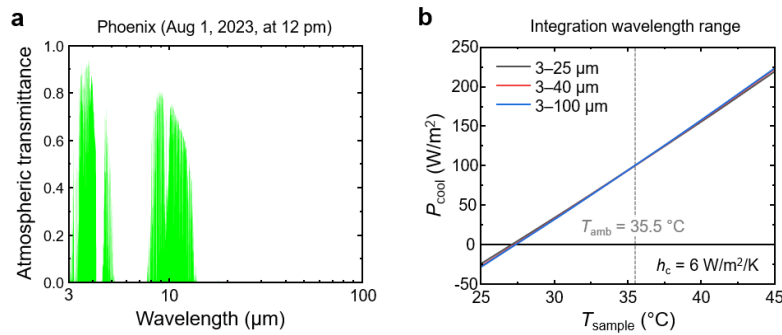


Figure S3. (a) Atmospheric transmittance spectrum in Phoenix (Aug 1, 2023, at 12 pm) with the wavelength range of 3–100 μm . There is almost no atmospheric transparency channel at wavelengths longer than 25 μm . **(b)** Net cooling power (P_{cool}) of an ideal broadband emitter (emissivity of 1 at wavelengths longer than 3 μm and of 0 elsewhere) in Phoenix, with three different wavelength ranges of 3–25, 3–40, and 3–100 μm . These ranges represent the integration wavelength range of P_{atm} in **Equation S1**. The ambient temperature (T_{amb}) of the same day and time was 35.5 $^{\circ}\text{C}$ and the heat transfer coefficient (h_c) was assumed to be 6

$W/m^2/K$. There is little difference in P_{cool} between the three wavelength ranges, and the difference is 0 at $T_{sample} = T_{emitter}$. As a result, it is reasonable to consider the wavelengths of 3–25 μm .

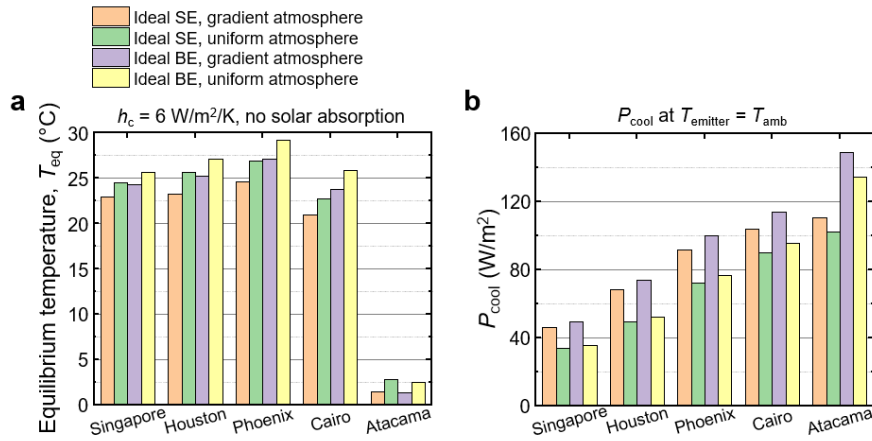


Figure S4. Comparison of the cooling performance of the ideal SE and BE between the uniform and gradient atmosphere, in the five selected locations. **(a)** The equilibrium temperature (T_{eq}) of the ideal SE and BE calculated by the two methods, and **(b)** the net cooling power P_{cool} at $T_{emitter} = T_{amb}$ calculated by the same methods. The conventional uniform atmosphere cases underestimate the cooling performance because the actual sky is cooler than the ambient temperature (T_{amb}).

Supplementary Note 4. Selective emissivity at 8–13 and 17–25 μm in the Atacama Desert

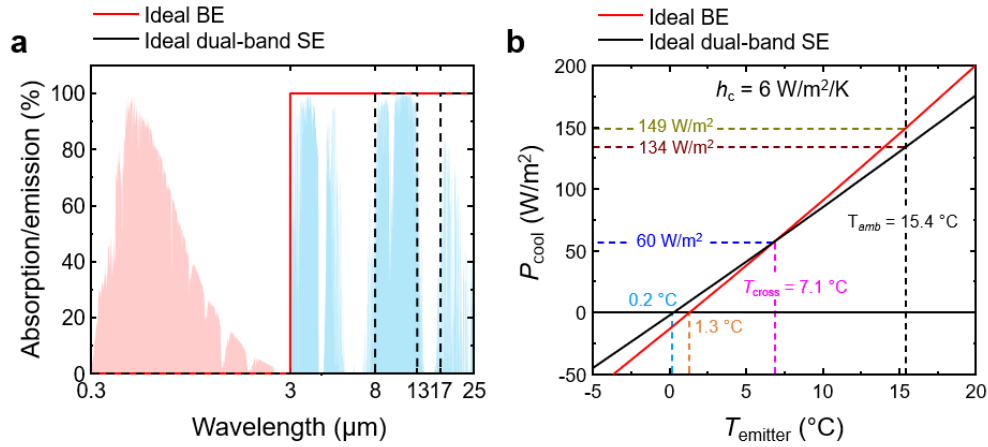


Figure S5. Ideal emitters in the Atacama Desert on Dec 1, 2023, at noon. **(a)** Emissivity spectra of the ideal BE (red solid line) and the ideal dual-band SE (black dashed line). The ideal dual-band SE shows high emissivity at wavelengths of 8–13 and 17–25 μm . **(b)** The net cooling power (P_{cool}) of the ideal BE (red line) and the dual-band SE (black line) as a function of the emitter temperature (T_{emitter}), with a heat transfer coefficient h_c of 6 $\text{W}/\text{m}^2/\text{K}$. The equilibrium temperature (T_{eq}) of the ideal dual-band SE (0.2 $^{\circ}\text{C}$) is lower than that of the ideal BE (1.3 $^{\circ}\text{C}$), but the difference in T_{eq} is only 1.1 $^{\circ}\text{C}$. The ideal dual-band SE has higher P_{cool} than the ideal BE only at a temperature range of 0.2 to 7.1 $^{\circ}\text{C}$, and the ideal BE has higher P_{cool} at temperatures higher than 7.1 $^{\circ}\text{C}$. When considering a practical operational temperature for sub-ambient cooling is within a few degrees from the ambient temperature ($T_{\text{amb}} = 15.4 \text{ }^{\circ}\text{C}$ in this case), (5, 6) the ideal BE may be usually better in the practical scenarios. In addition, the maximum P_{cool} , where the dual-band SE can be higher than the ideal BE, is below 60 W/m^2 , and the difference in P_{cool} at the 0.2~7.1 $^{\circ}\text{C}$ temperature range is also very small, below 10 W/m^2 . Note that in principle the exact optimal emissivity depends on the target emitter temperature but it is highly complex (7), making it almost impossible to experimentally demonstrate the emissivity in practice.

Supplementary Note 5. Optical properties of the actual SEs and BEs

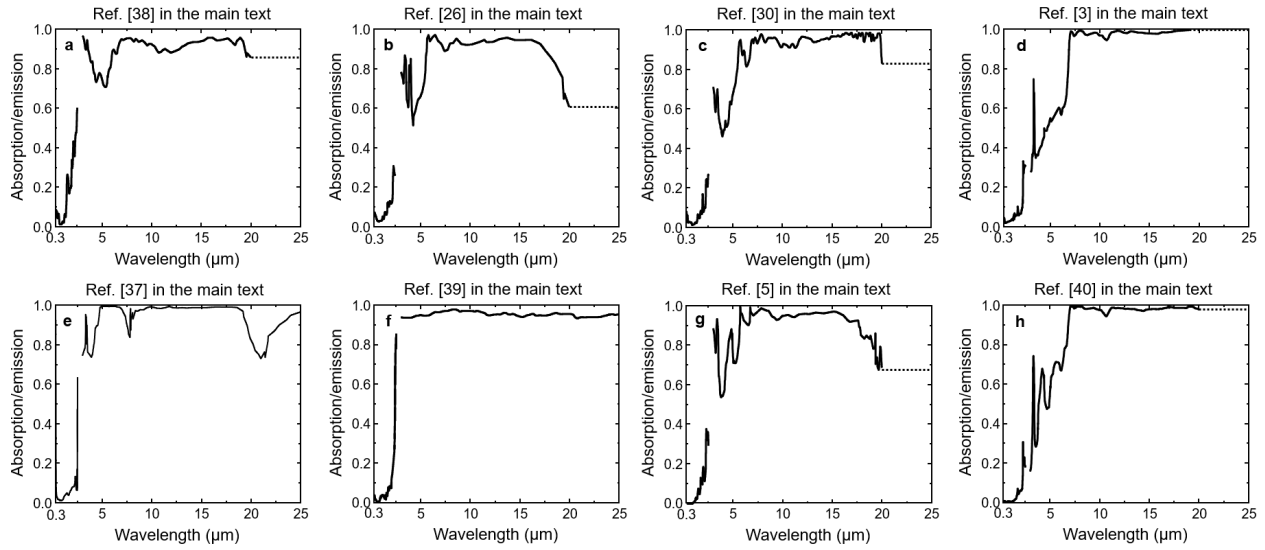


Figure S6. (a-h) Absorption/emission spectra of the actual BEs, and the reference papers can be found in the main text. The missing emissivities at 20–25 μm (dotted line) were extrapolated to the same emissivity value at 20 μm .

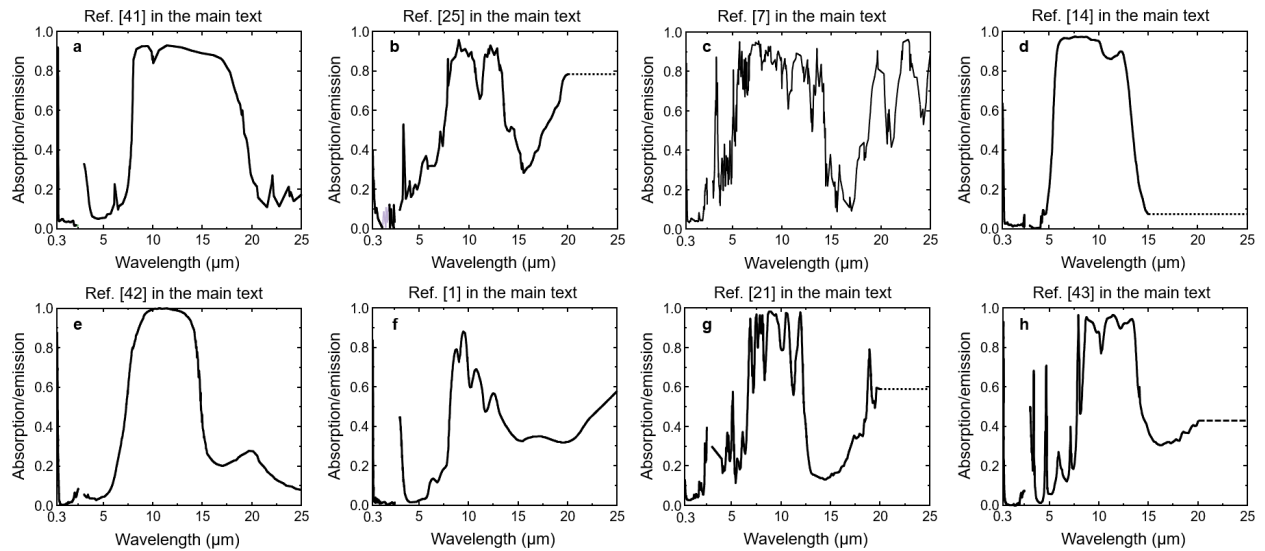


Figure S7. (a-h) Absorption/emission spectra of the actual SEs, and the reference papers can be found in the main text. The missing emissivities (dotted line) were extrapolated to the same emissivity value at 15 or 20 μm .

Supplementary Note 6. Cooling ability comparison between an active cooling system and a passive radiative cooling system

We compare the cooling abilities of two cooling systems: passive radiative cooling with an ideal emitter and an air conditioner (AC) powered by solar panels. The net cooling power (P_{cool}) of an ideal emitter is typically 50–100 W/m², and P_{cool} over a day is 1.2~2.4 kWh/m²/day, as the ideal emitter can be operated for 24 hours a day.

Let assume that the average solar irradiance in the United States during summer is 6 kWh/m²/day (8) and the efficiency of a solar panel is 20% (9). Then, it generates the electricity of 1.2 kWh/m²/day over a day. The cooling ability of an AC can be evaluated by seasonal energy efficiency ratio (SEER), which is given by:

$$\text{SEER} = \frac{\text{the cooling power during a typical cooling season (BTU)}}{\text{the total electricity input (Wh)}}, \quad (\text{S8})$$

where BTU is a british thermal unit. The minimum SEER requirements for residential systems set by the Department of Energy (DOE) is 14 BTU/Wh in 2023 (10). This SEER value corresponds to the efficiency of 410% when considering 1 BTU = 0.293 Wh. The cooling power of an AC powered by solar panels (1.2 kWh/m²/day) can be given by: $4.1 \times 1.2 \text{ kWh/m}^2/\text{day} = \underline{4.9 \text{ kWh/m}^2/\text{day}}$. So, the cooling power of the active cooling system is 2~4 times higher than that of the passive radiative cooler.

References

1. The NASA Planetary Spectrum Generator, <https://psg.gsfc.nasa.gov/>. (accessed 18 December 2023).
2. G. L. Villanueva *et al.*, *Fundamentals of the Planetary Spectrum Generator* (2022).
3. Gemini Observatory, <https://www.gemini.edu/observing/telescopes-and-sites/sites#Transmission>. (accessed Mar-19-2024).
4. A. P. Raman, M. A. Anoma, L. Zhu, E. Rephaeli, S. Fan, Passive radiative cooling below ambient air temperature under direct sunlight. *Nature* **515**, 540-544 (2014).
5. E. A. Goldstein, A. P. Raman, S. Fan, Sub-ambient non-evaporative fluid cooling with the sky. *Nature Energy* **2**, 1-7 (2017).
6. D. Zhao *et al.*, Subambient cooling of water: toward real-world applications of daytime radiative cooling. *Joule* **3**, 111-123 (2019).
7. S. Jeon, J. Shin, Ideal spectral emissivity for radiative cooling of earthbound objects. *Scientific Reports* **10**, 13038 (2020).
8. Solar Resource Maps and Data (National Renewable Energy Laboratory) <https://www.nrel.gov/gis/solar-resource-maps.html>.
9. Solar Panel Efficiency (MarketWatch); <https://www.marketwatch.com/guides/solar/solar-panel-efficiency/#:~:text=Most%20commercially%20available%20solar%20panels,of%2015%25%20to%2020%25>.
10. Efficiency requirements for residential central AC and heat pumps to rise in 2023 (U.S. Energy Information Administration). <https://www.eia.gov/todayinenergy/detail.php?id=40232>.